Lack of mucosal cholinergic innervation is associated with increased IL-23-induced T-helper-17 response in Hirschsprung's disease

Simone Keck[1*], Virginie Galati-Fournier[1], Urs Kym[1], Michèle Moesch[1], Jakob Usemann[2], Ulrike Subotic[1,3], Sasha J. Tharakan[3], Thomas Krebs[4], Eleuthere Stathopoulos[5], Peter Schmittenbecher[6], Dietmar Cholewa[7], Philipp Romero[8], Bertram Reingruber[9], Elisabeth Bruder[10], NIG study Group[11,12] and Stefan Holland-Cunz[1]

*Corresponding author: simone.keck@unibas.ch

[1] Department of Pediatric Surgery, University Children's Hospital Basel (UKBB) and University of Basel, Basel, Switzerland

[2] Department of Pediatric Pulmonology, University Children's Hospital Basel (UKBB), Basel and Division of Respiratory Medicine, University Children's Hospital Zurich, Zurich, Switzerland

[3] Department of Pediatric Surgery, University Children's Hospital Zurich, Zurich, Switzerland

[4] Department of Pediatric Surgery, Children's Hospital of Eastern Switzerland, St. Gallen, Switzerland

[5] Department of Pediatric Surgery, University Hospital of Lausanne (CHUV), Lausanne, Switzerland

[6] Department of Pediatric Surgery, Municipal Hospital, Karlsruhe, Germany

[7] Department of Pediatric Surgery, University Hospital of Bern, Bern, Switzerland

[8] Department of Pediatric Surgery, University Hospital of Heidelberg, Heidelberg, Germany

[9] Department of Pediatric Surgery, Florence Nightingale Hospital, Düsseldorf, Germany

[10] Department of Medical Genetics and Pathology, University Hospital Basel, Basel, Switzerland

[11] NIG Study Group: Isabella Bielicki[1], Sandra Weih[1], Ueli Moehrlen[3], Noëmi Zweifel[3], Kai-Uwe Kleitsch[4], Carole Gengler[12], Kiarasch Mortazawi[6], Milan Milosevic[7], Vera Otten[9], Lennart Homrighausen[9]

[12] Department of Pathology, University Hospital of Lausanne (CHUV) and University of Lausanne, Lausanne, Switzerland

Abstract

Hirschsprung's disease (HSCR) is a congenital intestinal motility disorder defined by the absence of enteric nervous cells (ganglia). The development of HSCR-associated enterocolitis remains a life-threatening complication. Absence of enteric ganglia implicates extramural innervation of acetylcholine-secreting (cholinergic) nerve fibers. Cholinergic signals have been reported to control excessive inflammation, but the impact on HSCR-associated enterocolitis is unknown. By grouping 44 HSCR patients according to their degree of mucosal cholinergic innervation, we provided evidence that extrinsic mucosal innervation correlated with reduced IL-17 cytokine levels and T-helper-17 (Th17) cell frequencies. Bipolar $CD14_{high}$ macrophages colocalized with neurons and expressed significantly less interleukin-23, a Th17-promoting cytokine. HSCR patients lacking mucosal cholinergic nerve fibers showed microbial dysbiosis and had a higher incidence of postoperative enterocolitis. The mucosal fiber phenotype might serve as a new prognostic marker for enterocolitis development in HSCR patients and may offer an approach to personalized patient care and new future therapeutic options.

Main

Hirschsprung's disease (HSCR) is a multigenetic congenital malformation of the colon characterized by a distal lack of enteric ganglia cells (aganglionosis) leading to intestinal obstruction and prestenotic megacolon. In affected infants, the aganglionic bowel part is surgically removed, and healthy ganglionic tissue is pulled through and reconnected to the anus. Either pre- or postoperatively, 20% to 50% of patients suffer from life-threatening HSCR-associated enterocolitis leading to acute abdominal distension, diarrhea, and fever up to sepsis and organ failure[1-3]. The underlying pathogenesis is not fully understood but appears to involve changes in intestinal barrier function[4-6], immune response[7-9], and the microbiome[10-15].

As a consequence of lacking an intrinsic enteric nervous system (ENS), extrinsic acetylcholine (ACh)-producing (cholinergic) nerve fibers originating from sacral roots S2-S4 innervate the distal colon. ACh released from these fibers is responsible for constant muscle contraction in HSCR patients[16].

Intestinal cholinergic signals not only coordinate physiologic bowel function but additionally prevent excessive inflammation by allowing the intestinal immune system to tolerate harmless commensals and food antigens[17]. The cholinergic-anti-inflammatory-pathway (CAIP) was first described by the Tracey group[18]. In a model of systemic inflammation, vagus nerve (VN) stimulation favored the release of ACh by memory T cells which in turn bound to α7-nicotinic ACh receptor (α7nAChR)-positive splenic macrophages (MΦ) to reduce tumor necrosis factor (TNF)-α production[18,19]. This concept was confirmed in intestinal inflammation models involving colitis[20-23], food allergy[24], postoperative ileus (POI)[25], and pancreatitis using VN stimulation or pharmacologic targeting of α7nAChR. In humans, nicotine, which

activates nAChRs, has been associated with clinical improvement of ulcerative colitis[26]. VN stimulation in Crohn's disease results in amelioration of disease activity[27]. Contrary to systemic CAIP, intestinal modulation is independent of the spleen and involves direct activation of local enteric neurons[25,28,29]. Although VN activation leads to downregulation of inflammatory cytokine production by muscularis MΦ via α7AChR activation in POI, it remains unclear which receptors and cell types are involved in colitis amelioration[30,31]. Given the fact that the ENS utilizes more than 30 different neurotransmitters, it is challenging to identify individual immune-modulating functions. As HSCR patients miss these ENS-specific neurotransmitters, the study of cholinergic neurons is possible.

Here, we investigated the role of cholinergic mucosal innervation in regulating the immune cell status, microbial composition, and development of enterocolitis in HSCR patients.

Results

Distinct cholinergic innervation of the colon in HSCR patients

In this prospective, multicenter study, we collected fresh tissue of different colonic segments from 44 pediatric HSCR patients undergoing therapeutic pull-through surgery as well as 6 control patients (non-HSCR) undergoing surgery for miscellaneous reasons. The length of aganglionic colon was determined by experienced pathologists of the respective pathology units (see Methods section, Supplementary Table 1 and Supplementary Table 2)[32]. Compared to non-HSCR colonic tissue, the aganglionic colon of HSCR patients lack the myenteric and submucosal plexus but show the characteristic increase of ACh esterase (AChE) activity in the rectosigmoid (Fig. 1a). Increased cholinergic activity is limited to the aganglionic rectosigmoid distal colon and decreases in caudocranial direction[16,33]. As a consequence, no extrinsic mucosal AChE+ nerve fibers can be detected in the proximal aganglionic colon descendens (CD), with only few present in the intermuscular space. Depending on the length of aganglionosis, the proximal CD segment of HSCR patients can be ganglionic or aganglionic (Fig. 1a and Supplementary Table 1). CD segments showing a hypoganglionic phenotype (transition zone) were excluded from the analysis.

We performed anti-AChE immunohistochemistry staining in cryosections of longitudinally rolled colonic stripes (Swiss roll), including rectum (REC), sigmoid colon (SC), and colon descendens (CD) from HSCR patients. All patient tissues showed the typical thick AChE+ fibers in the muscle region, but the density of thin mucosal fibers varied between patients (Fig. 1b, c). According to mucosal innervation in the distal rectosigmoid colon, the sections were semi-quantitatively

allocated into “fiber-low” (Fig. 1b) and “fiber-high” (Fig. 1c) patient groups in a double-blind investigation (see methods for details). Fiber phenotype was validated using tubulin immunohistochemistry (Supplementary Figure 1). Consequently, for further analysis, aganglionic and ganglionic segments with variable mucosal cholinergic innervation were defined as illustrated by anti-β3tubulin (pan neuronal marker) and anti-AChE (cholinergic marker) immunofluorescent staining (Fig. 2a). Thus, rectosigmoid fiber-low tissues were those lacking intrinsic nerve cell bodies as well as extrinsic mucosal cholinergic innervation. Rectosigmoid Fiber-high tissues were those lacking intrinsic nerve cell bodies but showing extrinsic mucosal cholinergic innervation (Fig. 2a, arrow). Aganglionic CD sections from HSCR patients were defined as those lacking intrinsic nerve cell bodies as well as extrinsic mucosal cholinergic innervation (because of extrinsic nerve fiber restriction to the rectosigmoid). Hence, aganglionic CD segments were used from both fiber-low and fiber-high patient tissue. Ganglionic CD sections from HSCR and non-HSCR patients showed the presence of non-cholinergic intrinsic nerve cell bodies (ganglia) with mucosal nerve terminals (Fig. 2a, asterisk) and were considered as normally innervated. Secondary antibody controls showed a high background in the epithelial crypt region for AChE due to biotin/streptavidin amplification (Fig. 2d). By performing immunofluorescence studies in fiber-high tissue, we could exclude peptidergic (VIP), dopaminergic/adrenergic (TH), and nitrinergic (NOS) origins of the mucosal fibers (Fig. 2b). However, we detected TH_+ nerve bundles in the submucosa and muscle region. Sporadic fiber bundles were positive for the glia cell marker S100B, and the majority of mucosal fibers were not associated with glia cells (Fig. 2b). Respective secondary antibody controls were negative (Fig. 2c). We did not observe any significant patient bias in terms of anthropometric, clinical, environmental, or

maternal factors between fiber-low and fiber-high tissues, except a higher percentage of infants delivered by cesarean section in the fiber-high patient group (Supplementary Table 3).

Absence of cholinergic fibers correlated with inflammatory immune status

A functional ENS is crucial for intestinal immune homeostasis[34]. To investigate if the absence of neuronal signals impairs the overall inflammatory cytokine status in HSCR patients, we performed quantitative real-time polymerase chain reaction (q-RT PCR) analysis as well as Luminex analysis of whole colonic tissue from HSCR patients and control patients. On the RNA expression level, TNF-α did not significantly vary between the different colonic segments from HSCR patients and control patients (Fig. 3a). Cytokines involved in Rorγt^{+} Th17 cell differentiation, i.e., IL-1β, IL-23, and IL-6[35,36], were significantly elevated in aganglionic CD segments compared to ganglionic CD segments, but they were not significantly changed compared to fiber-high segments. IL-17 and IL-22, two Th17 effector cytokines, were significantly elevated in aganglionic CD sections compared to ganglionic CD sections from HSCR patients (Fig. 3a). Both cytokines were significantly attenuated in cholinergically innervated fiber-high segments compared to fiber-low or aganglionic CD segments. On the protein level, TNF-α and IL-1β were significantly increased in aganglionic compared to ganglionic CD segments (Fig. 3b). None of the tested cytokines were significantly different between aganglionic fiber-low and fiber-high segments (Fig. 3b). However, IL-17 protein levels tended to be elevated in aganglionic fiber-low tissue compared to fiber-high tissue showing the lowest p value ($p=0.123$) of all tested cytokines (Supplementary Table 4).

Beside innate lymphoid cells 3 (ILC3) and others, Th17 cells are the main producers of IL-17 and IL-22 and are counter-regulated by forkhead box P3 positive (Foxp3^{+}) regulatory T cells (Treg)[37-40]. Frequencies of mucosal IL17^{+} Th17 and Foxp3^{+} Treg T cells were assessed by flow cytometry (Fig. 3 c, d, supplementary Fig. 3a, b). Th17 frequencies were significantly increased in fiber-low segments compared to fiber-high segments or CD segments (Fig. 3c, Supplementary Fig. 2a showing the percentage of total cells). We observed no difference between aganglionic and ganglionic CD tissue of HSCR and control patients. Treg frequencies were significantly elevated in both fiber-low and fiber-high tissues from HSCR patients (Fig. 3d, Supplementary Fig. 2a showing the percentage of total cells). However, the ratio of Th17/Treg was significantly higher in fiber-low segments compared to fiber-high segments (Fig. 3e, Supplementary Fig. 2a showing the percentage of total cells). Frequencies of natural killer (NK) cell receptors (NCR)$^{+}$ and NCR^{-} ILC3s were comparable between fiber-low and fiber-high tissues from HSCR patients. However, the NCR^{-} ILC3 population was significantly elevated in fiber-low colonic segments compared to ganglionic CD of HSCR patients (Supplementary Fig. 2b). Thus, lack of an ENS appeared to have an impact on inflammatory cytokine production, whereas lack of cholinergic neurons seemed to affect Th17 cells and their related cytokines.

CX3CR1^{+} MΦ represent the major antigen-presenting cell (APC) type in the colon and are crucial for CD4 T cell differentiation[41]. These MΦ exhibit a non-inflammatory M2-like phenotype and are essential for local expansion and maintenance of Treg[42,14]. In contrast, intestinal CCR2^{+} CX3CR1^{+} blood-monocyte-derived MΦ are essential for Th17 cell differentiation[43-47]. We performed qRT-PCR analysis in whole colonic tissue to check for expression of CX3CR1 and CCR2. In fiber-high tissue as well as in muscle tissue, we found a significantly higher expression of CX3CR1 than

CCR2 while in all other segments, expression levels of the two markers were comparable (Supplementary Fig. 2c). To check whether these changes resulted from altered MΦ populations, we investigated viable CD64^{+} MΦ by flow cytometry (Supplementary Fig. 3d). All MΦ expressed comparable levels of CD11c (Fig. 3f, upper graph). However, we found a significantly higher expression of CD14, an M2 marker[48], in MΦ isolated from the mucosal lamina propria (LPMΦ) of fiber-high colonic tissue and in MΦ isolated from muscularis (MMΦ) (Fig. 3f, lower graph). MMΦ interact with neurons of the myenteric plexus and have been described as bipolarly shaped[49-51]. Using confocal fluorescence microscopy, we visualized a bipolar shape of LPMΦ in fiber-high segments similar to that seen with MMΦ (Fig. 3g, left and right image). In contrast, LPMΦ in fiber-low colonic segments exhibited a round or stellate phenotype (Fig. 3g, middle image). We found a significantly higher percentage of bipolar MΦ in fiber-high colonic tissue (Fig. 3g, bar graph). We mimicked the phenotype of the two colonic macrophage populations by differentiating blood-derived monocytes from healthy adult donors into M1 and M2 MΦ. After 10 days of differentiation, M2 MΦ showed an elongated bipolar shape (Supplementary Fig. 2d, e) and increased expression of CD14 and CX3CR1 (Supplementary Fig. 2f, g). In contrast, M1 MΦ exhibited a rounded shape and expressed moderate levels of CD14 while lacking CX3CR1 expression. To test the ability of the MΦ to differentiate T cells into certain effector T cells, we co-cultured M1 and M2 MΦ with autologous naïve CD4 T cells in the presence of anti-CD3 and performed a Th17 and Treg T cell differentiation assay. After 6 days of co-culture, the frequency of Th17 and Treg cells were analyzed and the ratio calculated. Th17/Treg ratio was significantly lower when bipolar CX3CR1^{+}CD14^{high} M2 MΦ were used (Supplementary Fig. 2h). These observations suggested that fiber-high

segments of HSCR colon harbor a bipolar $CD64^{+}CD11c^{+}CD14^{high}$ MΦ population in the mucosa, presumably in a way similar to that seen with M2 MΦ differentiated *in vitro*, with decreased capacity to induce Th17 cells. Of note, due to the low viability of patient-derived colonic macrophages, no functional assays could be performed, and M2 MΦ did not fully resemble the colonic phenotype.

Bipolar $CD14^{high}$ MΦ colocalized with cholinergic fibers

Both MΦ and T cells express receptors for neurotransmitters, qualifying them for neuronal interaction[25,49,50,52-54]. Representative fluorescence images (20x and 63x) of fiber-high and fiber-low distal colonic tissue revealed $CD64^{+}$ MΦ and $CD3^{+}$ T cells in close neighborhood to $AChE^{+}$ fibers (Fig. 4a). In the muscle layer, MΦ were only detected between thick cholinergic fibers. To identify the cell type interacting with mucosal nerve fibers, we performed fast-scanning confocal imaging using a Fiji software macro to determine the sum of overlapping pixel values (Fig. 3b and Supplementary Movie 1). Per patient (fiber-low segments, n=4; fiber-high segments, n=5; muscle, n=2), 100-200 cells were annotated, and the sum of pixel values was determined. The results showed that LPMΦ in fiber-high segments significantly colocalized with cholinergic fibers comparable to MMΦ, in contrast to LPMΦ of fiber-low segments (Fig. 4c). No significant overlap between $CD3^{+}$ T cells and cholinergic fibers was found (Fig. 4d). Furthermore, neuron-associated LPMΦ in fiber-high tissue from HSCR patients mainly exhibited a bipolar shape (Fig. 4e). These results suggest that bipolar LPMΦ preferentially interacted with cholinergic fibers in aganglionic fiber-high tissue from HSCR patients.

Cholinergic fibers suppressed Th17 inducing IL-23 expression in MΦ

We next sought to identify specific genes targeted by neuronal interaction. Therefore, we performed RNA sequencing in viable FACS sorted mucosal MΦ ($CD45^+HLA^+CD64^+$) from fiber-low and fiber-high tissues. As control, we included MMΦ as well as blood-derived M1 and M2 MΦ differentiated *in vitro*. Principal component analysis (PCA) showed clear transcriptional separation of blood-derived M1 and M2 MΦ, whereas colonic LPMΦ and MMΦ accumulated together (Fig. 5a). Macrophage-specific genes (CD64, CD14, ITGAM, CX3CR1, CCR2, ITGAX, and CSF1R) were similarly expressed between colonic populations while MMΦ expressed muscle-specific Lyve1 (Fig. 5b)[55]. When testing for gut-specific M2 markers (AhR, CD200R1, AREG, CD209, TGF-β2, and IL-10), we found elevated expression in colonic subsets similar to blood-derived M2 MΦ. In contrast to LPMΦ from fiber-low segments, LPMΦ from fiber-high tissue as well as MMΦ showed decreased expression of chemokine receptor CCR7 crucial for lymph-node homing, indicating a tissue-resident population (Fig. 5b). Differential gene expression analysis yielded 24 significantly changed genes between LPMΦ isolated from fiber-low and fiber-high colonic tissues (Fig. 5c, d). Strikingly, IL-23a, a subunit of the Th17-inducing cytokine IL-23, was significantly downregulated in LPMΦ from fiber-high segments, suggesting a correlation to cholinergic innervation. Additionally, we found a significant reduction of IL-6 and CCL-20, both of which are involved in Th17 differentiation and recruitment, but no significant change in TNF-α (Fig. 5e).

Using immunofluorescence analysis, we quantitatively analyzed IL-23 protein expression in $CD64^+$ LPMΦ in cryosections from fiber-low and fiber-high colonic tissue (Fig. 5f, g). LPMΦ in 4 to 8 regions per patient were analyzed and quantified using CellProfiler software. Fiber-low colonic tissue showed significantly increased frequencies of IL-23-positive LPMΦ compared to fiber-high colonic tissue (Fig. 5h).

This result indicated that the lack of mucosal cholinergic fibers correlated with increased expression of the Th17 inducing cytokine IL-23 in LPMΦ.

Distinct expression of macrophage-neuron crosstalk transcripts

Next, we aimed to identify receptors possibly involved in the neuronal modulation of LPMΦ. Based on transcriptional analysis, we verified the expression of receptors for neurotransmitters, neuropeptides, neurotrophic factors, and axon-guidance proteins (Fig. 6). Considering the crucial role of α7nAChR in mediating the CAIP, we found elevated levels of the receptor in LPMΦ isolated from fiber-high segments from HSCR patients (Fig. 6a and f). In contrast, other receptors reported to be involved in cholinergic immune suppression such as receptors for serotonin[56], catecholamine (ADRB2)[50,57], or neuropeptides (NMUR1, VIPR1, SSTR2, and CALCRL)[58-65] were not upregulated in fiber-high LPMΦ compared to fiber-low LPMΦ or were not expressed (NMUR1) (Fig. 6b, c and f). MΦ secrete different neurotrophic and axon-guidance proteins as well as respective receptors. Fiber-associated LPMΦ expressed growth/differentiation factor (GDF) 15 and, to a lesser extent, GDF11 (Fig. 6d and f). Within the family of axon-guidance proteins, we found elevated expression of the receptors neuropilin-1 (NRP1), UNC-5 homology B (UNC5B), and ephrin type B-receptor 2 (EPHB2) binding semaphorin 3A (SEMA3A), netrin, and ephrin-B family members, respectively (Fig. 6e and f). In contrast, LPMΦ isolated from fiber-low segments showed elevated expression of SEMA3A and SEMA7A compared to LPMΦ from fiber-high segments (Fig. 6e and f).

Overall, these data suggest a possible involvement of α7nAChR in neuron- MΦ crosstalk. In addition, fiber-associated MΦ seemed to support neuronal growth and differentiation via GDF production and axon-guidance proteins. However, data

analysis was limited by low sample numbers and high variance and thus needs further validation.

Microbial dysbiosis in colonic fiber-low tissues from HSCR patients

Lacking intestinal MΦ or ENS affects the composition of intestinal microbiome[66-69]. In a chemically induced colitis model in mice, CX3CR1$_{+}$ MΦ were crucial to maintain the intestinal barrier function to prevent bacterial translocation[47,70]. To evaluate if the presence of cholinergic fibers impacts on bacterial translocation, we performed 16S rDNA FISH analysis of fiber-low and fiber-high cryosections. Bacteria translocated to lamina propria were detected in both groups, but no significant difference was found (Supplementary Fig. 4a, b). We then checked the composition of microbial communities by 16s rDNA sequencing in cryosections of fiber-low, fiber-high, and ganglionic CD tissue from HSCR patients. Alpha diversity analysis showed an increase in operational taxonomic units (OTUs) in fiber-low tissue when compared to ganglionic CD tissue, whereas estimated OTU richness as well as beta diversity were comparable in all groups (Fig. 7a and Supplementary Fig. 4c). On the phylum levels, *Actinobacteria* seemed to be less prevalent in aganglionic tissue compared to ganglionic tissue (Fig. 7b). Within the bacterial family compositions, *Actinobacteria* were significantly less prevalent in fiber-low segments compared to ganglionic CD, whereas other families were similarly expressed (Fig. 7c). The main representative species of the *Actinobacteria* were several *Bifidobacteria* (*B. longum* (OTU1)*; B. bifidum* (OTU6)*; B. pseudocatenulatum* (OTU5), with *B. longum* showing the highest frequency in all samples (Supplementary Table 5). Differential bacterial family analysis between fiber-low and fiber-high colonic tissue revealed a significant increase in *Staphylococcaceae* in fiber-low colonic segments, whereas in fiber-high tissue, *Enterobacteriaceae* and *Clostridiales Family_XI* were upregulated (Fig. 7c).

Within the *Staphylococcaceae* family, *S. aureus* (OTU7) was the only detectable species within the core microbiome (Supplementary Table 5). The *Clostridiales Family_XI* was represented by 4 genera, i.e., *Finegoldia* (OTU825)*, Peptoniphilus* (OTU196)*, Anaerococcus* (OTU543) and *Ezakiella* (OTU27, OTU63). The main representative species of *Enterobacteriaceae* family was *Escherichia coli* (OTU2), which represented the second frequent bacterial species from the core microbiome (Supplementary Table 5). These observations suggested a different composition of colonic translocated bacteria between fiber-low and fiber-high tissue including a decrease in *Actinobacteria* and prevalence of *Staphylococcaceae* family in fiber-low segments lacking cholinergic mucosal innervation.

HSCR patients with fiber-low phenotype showed a higher incidence of post-operative enterocolitis

Next, we evaluated the impact of fiber phenotype on the development of postoperative enterocolitis. One year after pull-through surgery, 42 HSCR patients were followed up, and postoperative enterocolitis manifestation was evaluated from medical records. Enterocolitis was defined to fulfill at least 3 of the following criteria: diarrhea (>3x/day), vomiting, temperature >38.5°C, antibiotics, hospitalization, meteorism, and high inflammatory blood parameters (i.e., leucocytes, CRP). Anthropometric, clinical, environmental, maternal, and dietary factors, collected from the parent questionnaire, were analyzed for potential enterocolitis risk factors. A total of 9 (of 42) patients developed enterocolitis one year after surgery (Table 1a). Development of enterocolitis was significantly associated with cesarean delivery at birth of the infant (p=0.012). Seven of the 9 patients exhibited a fiber-low and only two a fiber-high phenotype, showing a higher incidence of fiber-low phenotype among the children who developed enterocolitis (78% versus 22%, p=0.634). To

validate the observations, we analyzed a retrospective HSCR patient cohort collected between 2003 and 2018 at the UKBB (Supplementary Table 6). A total of 29 HSCR patients were included. We did not observe any significant patient bias in terms of anthropometric or clinical factors between fiber-low and fiber-high tissues (Supplementary Table 7). Enterocolitis development was recorded in 14 of 29 patients but showed no correlation with anthropometric or clinical data (Table 1b). Strikingly, enterocolitis development correlated significantly with the fiber phenotype showing a higher incidence in children with the fiber-low phenotype (86%, 12/14 children) compared to the fiber-high phenotype (14%, 2/14). These observations suggest that HSCR patients with fiber-low phenotype might have a higher risk to develop enterocolitis and that the fiber phenotype could serve as a prognostic marker for risk of enterocolitis development.

Discussion

In recent years, multiple studies mainly using different mouse disease models demonstrated the reciprocal relationship between immune and nervous systems. In humans however, difficulty to study individual effects of neurotransmitters leads to a lack of studies providing direct evidence of neuronal-immune crosstalk. Here, we provided unique evidence of a cholinergic neuron-macrophage crosstalk in the colon correlated with reduced type 17-mediated immune reactions. By studying colonic tissue of HSCR patients characterized by the lack of an ENS and extramural mucosal cholinergic innervation, we deciphered the relationship between neuronal ACh and the mucosal immune system. Using confocal colocalization studies, we identified elongated tissue-resident MΦ interacting with cholinergic nerve fibers. Differently shaped intestinal MΦ populations were described before. Gabanyi et al. described bipolar-shaped MMΦ with a tissue-protective anti-inflammatory M2 phenotype contrary to stellate-shaped LPMΦ[50]. The elongated profile allows MMΦ to interact and wrap around neighboring neurons. At steady state, MMΦ regulate ENS functions and therefore gut motility by providing bone morphogenetic protein (BMP) 2 in response to microbial stimuli[49]. Tamoxifen-induced deletion of CX3CR1$_+$ tissue-resident MΦ leads to loss of enteric neurons[71]. Interestingly, MMΦ develop independently of the ENS[71,72]. The ENS supplies colony-stimulating factor1 (CSF1) needed for M2 MΦ differentiation and survival[49,73]. Upon *Salmonella typhimurium* infection, MMΦ interact with sympathetic adrenergic neurons via β2 adrenergic receptors to induce a tissue- and neuron-protective gene expression program[50]. In a model of POI which is characterized by surgery-induced inflammatory response of MMΦ and impaired motility, VN stimulation or pharmacologic triggering of cholinergic enteric neurons prevented MΦ activation and reduced POI in a α7nAChR-dependent

manner in both mice and humans[56]. However, anti-inflammatory neuro-immune modulation seems to involve different neuronal receptors in type 2-mediated intestinal disease models. For example, in a murine model of food allergy, VN stimulation ameliorated disease severity independently of α7nAChR[74]. Uptake of food antigens by anti-inflammatory CX3CR1^{+} MΦ and subsequent induction of food-specific Tregs effectively prevent allergic reactions[44]. VN stimulation increases phagocytic activity in CX3CR1^{+} MΦ, independently of α7nAChR, but phagocytic activity remains dependent on α4β2nAChR[75]. Using a murine helminth infection model, the Artis group demonstrated that the cholinergic neuropeptide neuromedin U activates ILC2 thus increasing the protective immune response and parasitic clearance[58,59]. In contrast, signals from sympathetic adrenergic neurons lead to attenuated ILC2 effector function and prevent chronic pathologic type 2 inflammation via activation of ILC2-specific β2 adrenergic receptors[76]. In our study, IL-23, a cytokine promoting the maintenance of Th17 cells[77], is significantly increased in LPMΦ isolated from fiber-low tissue lacking cholinergic innervation compared to innervated fiber-high tissue. Consistent with this finding, elevated Th17 cells were detected in fiber-low colonic tissue compared to fiber-high colonic tissue. Th17 cells are indispensable for the clearance of extracellular bacteria and fungi and therefore for protective immunity. Dysregulation of cytokines controlling Th17 cells predisposes to the development of autoimmune diseases and inflammatory bowel disease[36,78,79]. Genome-wide studies identified genes, including the gene for IL-23 receptor, involved in Th17 differentiation associated with a susceptibility to inflammatory bowel disease[78,80-82]. IL-23 is produced by dendritic cells and MΦ in response to extracellular bacteria and fungi recognized by special innate pattern-recognition receptors, the toll-like receptor (TLR) 2 and nucleotide oligomerization

domain containing protein 2 (NOD2)[83,84]. Under inflammatory conditions, monocyte-derived CCR2+CX3CR1+ MΦ infiltrate the gut mucosa and prime Th17 cell responses[43,47]. At steady state, CX3CR1+ MΦ are indispensable for epithelial integrity, control of bacterial translocation, and development of oral and commensal tolerance by secreting anti-inflammatory cytokines and maintaining Treg[44,68]. CX3CR1 MΦ further promote intestinal homeostasis by microbiota-dependent crosstalk with IL-22-secreting ILC3[85].

In our study, we found higher tissue expression of CX3CR1 than CCR2 in fiber-high colonic segments of HSCR patients and identified two MΦ populations based on CD14 expression and shape. CD14+ bipolar MΦ were found in close proximity to nerve fibers in both muscularis and lamina propria, expressing low levels of CCR7, suggesting a tissue-resident phenotype[86]. CD14low stellate-shaped MΦ were present in non-innervated lamina propria tissue, expressing CCR7 indicating a migratory population. Based on their transcriptional profile, LPMΦ isolated from both fiber-low and fiber-high colonic tissues exhibit a gut-imprinted M2 phenotype (CX3CR1, AREG, AhR, CSF1R, CD200R, CD209, TGFβ2, and IL-10), but they differed in Th17 cytokines (IL-23 and IL-6) and Th17 chemokines (CCL20). Consequently, cholinergic signals seemed to be associated with reduced type 17 immune responses. In a murine model of psoriasis, sensory nociceptive neurons augment dermal dendritic cell-mediated IL-23 production[64]. The neurons directly sense disease-inducing *Candida albicans* and release the neuropeptide calcitonin gene-related peptide (CGRP) which increases IL-23 production[65]. Surprisingly, another study uncovered an immunosuppressive effect of nociceptive fibers during *S. aureus* infection indicating a role for the properties of the underlying pathogen or target immune cell on nerve fiber-induced immune modulation[87].

Neurotrophic factors and their respective receptors are crucial for ENS development and function. In fact, the underlying genetic defects in HSCR patients involve signaling pathways controlling migration and development of the ENS, including the two major HSCR genes, rearranged during transfection (Ret) and endothelin receptor type B (EndrB)[88,89]. In a study using Ret-deficient mice, the authors demonstrated that microbiota-induced glial cell-derived neurotrophic factors induce IL-22 in Ret-expressing ILC3 therefore maintaining intestinal homeostasis[90]. Ret expression was not detected in colonic MΦ populations, and we did not detect any changes in ILC3 frequencies between fiber-low and fiber-high colonic segments. Here, we used RNA-seq transcriptional analysis to identify factors and receptors involved in neuro-immune interactions. However, the RNA-seq data were highly variable within the groups and were not validated in qPCR analyses or on protein levels. Further studies are needed to fully uncover receptors and mechanisms involved in neuron-MΦ interactions. Besides the contribution of cholinergic receptors, we supposed the contribution of neurotrophic factors, axon-guidance proteins, and their respective receptors in neuron-MΦ interactions. GDF15 has been reported to suppress inflammatory responses in a murine model of endotoxin-induced sepsis and prevent maturation of inflammatory dendritic cells in a heart-transplantation model[91,92]. Using an imiquimod- or IL-23-induced mouse model of psoriasis-like skin inflammation, GDF11 administration attenuated the severity of skin inflammation via suppression of the NF-κB signaling pathway[93]. Recently, NRP-1 was identified in adipose-tissue MΦ protecting from metabolic syndrome by favoring fatty acid uptake and β-oxidation away from pro-inflammatory M1 polarization and glycolysis[94]. Additionally, in a model of a neurodevelopmental disorder, brown adipose-tissue MΦ

control sympathetic tissue innervation critical for thermogenesis via the plexin-semaphorin pathway[52].

Inflammation in chemically induced colitis is suppressed by administering recombinant netrin-1[95] whereas UNC5B deficiency exacerbates chemically induced colitis[96]. SEMA3A regulates neurite growth cone repulsion suggesting a role of LPMΦ from fiber-low tissues in the inhibition of mucosal innervation[97,98]. Besides its crucial role in neurogenesis, SEMA7A supports the generation of monocyte-derived inflammatory cytokines and differentiation of inflammatory T cells[99,100]. More studies are needed to evaluate the involvement of the different receptors in our study.

The microbial composition of feces from HSCR patients with enterocolitis is shifted towards opportunistic pathogens such as *Candida albicans* und *Clostridium difficile*[1,10,101,102]. In our study, none of the patients was diagnosed with enterocolitis at the time of the pull-through surgery. However, higher baseline frequencies of Th17 cells and IL-23 might promote *C. difficile* infection, as was recently postulated[103]. Microbial prevalence and composition were altered in aganglionic tissue from fiber-low and fiber-high phenotypes compared to ganglionic segments. *Actinobacteria* were significantly reduced in fiber-low segments compared to ganglionic CD tissue. Compared to fiber-high colonic tissue, fiber-low tissue is associated with higher levels of *Staphylococcus aureus* previously reported to be associated with an increased Th17 response[104]. In contrast, *Clostridiales Family_XI* was upregulated more than 2 log2 fold in fiber-high tissue compared to fiber-low tissue, which was associated with a decreased risk of *Clostridium difficile* infection and necrotizing enterocolitis in preterm children[105,106]. In our study, differential bacterial analysis was limited due to the small patient samples per group and high variability within the

groups. The fact that we analyzed bacterial communities in colonic tissue and rather than feces further limited the data analysis.

Overall, 9 of 42 patients developed HSCR-associated enterocolitis one year after pull-through-surgery. Interestingly, development of enterocolitis was significantly associated with cesarean delivery at birth of the infant in the prospective HSCR patient cohort. Microbial composition in children delivered by cesarean section is known to be associated with skin commensals such as *Staphylococcus*, while the microbiome in children delivered by natural birth mode is characterized by vaginal bacteria, *e.g., Bifidobacteria* and *Lactobacillus*[107-110]. However, since cesarean section was not a significant risk factor in the retrospective patient cohort, its role in enterocolitis development needs to be further examined. Analyzing the correlation of fiber phenotype with enterocolitis development one year after pull-through surgery showed a higher incidence for fiber-low (78%) phenotype than fiber-high (22%) phenotype in patients developing enterocolitis. The result was validated in a retrospectively analyzed HSCR patient cohort and showed a significant incidence of 86% (fiber-low phenotype) versus 14% (fiber-high phenotype) to develop enterocolitis. In the retrospective cohort, fiber-low and fiber-high phenotypes were equally distributed (15 versus 14). Almost 50% of the study population developed enterocolitis compared to 21% in the prospective cohort.

HSCR represents a rare disease, and low patient numbers limit data analysis. However, we anticipate validating our results in additional retrospective HSCR patient cohorts. Interestingly, in HSCR mouse models using EndrB-deficient mice, no mucosal nerve fibers were detected, and the mice exhibited microbial dysbiosis leading to enterocolitis[111-113]. The absence of cholinergic fibers could therefore serve as a predictive marker for enterocolitis and improve personalized patient

management. With the current post-operative therapeutic management, clinicians can react to inflammatory bowel situations only at the time point of enterocolitis onset. Using the fiber phenotype as a prognostic marker for the risk of enterocolitis, clinicians could directly react after pull-through surgery to prevent postoperative enterocolitis. Possible therapies include high-volume enemas, antibiotic interval treatment, pre- and probiotic therapy, as well as dietary adaptations. Additionally, interventional surgical corrections may be considered. For instance, it is still unclear how the neuronal phenotype of a resected colon segment might predispose for enterocolitis development. It has been reported that colonic inflammatory Th17 cells migrate to neighboring mesenteric lymph nodes, triggering enterocolitis development. Because the mesentery is generally not removed during surgery, this could explain why patients may develop enterocolitis after removal of affected aganglionic colon segments. Using the fiber phenotype as a prognostic enterocolitis marker would enable possible resection of the neighboring mesentery lymph nodes/tissue as a strategy to prevent enterocolitis. Further, immunotherapies targeting IL-17 or IL-23 rather than TNF-α could open new therapeutic treatment options.

Using a HSCR patient cohort lacking the ENS, we provided evidence that extrinsic mucosal cholinergic neurons interacted with MΦ and correlated with reduced type-17 immune response most likely mediated by reduced MΦ-dependent IL-23 expression. HSCR patients lacking mucosal extrinsic cholinergic neurons had a higher risk of developing postoperative enterocolitis. The mucosal fiber phenotype could serve as a new prognostic marker for HSCR-associated enterocolitis risk and may offer a personalized patient care and future therapeutic options.

Methods

Patients and human specimens

A total of 44 children (median age 5 months) with HSCR as well as miscellaneous intestinal diseases (non-HSCR, control group) were enrolled in a prospective multicenter study conducted in Switzerland and Germany. The study was approved by the Ethics Committees of Northwest/Central Switzerland (EKNZ 2015-049) and the Medical Faculty Heidelberg (S-388/2015). The study was registered at www.clinicaltrials.gov (accessing number NCT03617640) and was performed according to the Declaration of Helsinki. After obtaining consent, colonic tissue was collected freshly in the operating room. For histological analysis, a longitudinal strip of resected colonic tissue was immediately snap-frozen. Tissue for RNA analysis was stored in RNAlater (Qiagen) or immediately frozen on dry ice. Tissue for fluorescence-activated cell sorting (FACS) analysis was kept on ice in Hanks' Balanced Salt Solution (HBSS) supplemented with 100 units penicillin, 0.1 mg/mL streptomycin, 0.25 µg/mL amphotericin B, and 40 µg/mL gentamycin and was processed in less than 24 h. The HSCR group included patients with short-segment (n=31), long-segment (n=6), and total (n=7) colonic aganglionosis. Surgery was performed according to the Swenson or Soave technics (Supplementary Table 1)[114-116]. The length of aganglionosis was determined intraoperatively in mapping biopsies, and postoperatively in the resected tissue via enzyme-histochemical staining. Tissue staining and assessment were performed by the pathology units of the respective clinics (Supplementary Table 2). Ganglionic tissue was characterized by the presence of intrinsic nerve cell bodies. The presence of intrinsic nerve cell bodies (ganglia) was detected by several enzymatic stainings: lactic dehydrogenase (LDH), succinic dehydrogenase (SDH), nitroxide synthase (NOS), nicotinamide adenine

dinucleotide phosphate (NADPH), and immunohistochemical calretinin staining (Supplementary Table 2). Aganglionic tissue was characterized by the lack of intrinsic cell bodies and presence of extrinsic nerve fibers in the distal colon. Extrinsic nerve fibers were detected by enzymatic acetylcholinesterase (AChE) staining (Supplementary Table 2)[16,33]. Study group characteristics (clinical and nonclinical variables) were evaluated via a parent questionnaire. Postoperative symptoms (obstipation, incontinence, enterocolitis, and pain) as well as postoperative treatments (laxative, clyster, botox, antibiotics, colonic irrigation, and pre-/probiotics) were evaluated from medical records one year after surgery. Enterocolitis was defined to fulfill at least 3 of the following criteria: diarrhea (>3x/day), vomiting, temperature >38.5°C, antibiotics, hospitalization, meteorism, and high inflammatory blood parameters (i.e., leucocytes, C-reactive protein (CRP)). For the retrospective cohort analysis, we included HSCR patients diagnosed and treated at the University Children's Hospital Basel between 2003 and 2018. Patients were identified using International Classification of Disease (ICD-10) Diagnosis Q43.1. Swiss roll cryosections (5 µm) from resected distal aganglionic colon were provided by the Department of Pathology, University Hospital Basel, Basel, Switzerland. Fiber scoring was performed using beta III tubulin immunohistochemistry and evaluated in a double-blind fashion by three individuals. Demographic and clinical data were extracted from medical records. Enterocolitis was defined in the same way as in the prospective cohort study. The study was approved by the Ethics Committee of North-West-Switzerland (EKBB 2019-01406).

Immunohistochemistry and nerve fiber scoring

Longitudinal colonic strips were washed in ice-cold phosphate buffered saline (PBS) and embedded as a Swissroll in Tissue-Tek® O.C.T. Compound (Sakura).

Cholinergic nerve fibers were visualized in 5 µm cryosections using mouse IgG2b anti-human AChE (Abcam) or mouse IgG2a anti-human beta III tubulin antibody together with an anti-mouse HRP-AEC staining kit (R&D) according to instruction manuals. Slides were automatically scanned using an Olympus BX63 motorized brightfield microscope using a 10x objective. Presence of extrinsic nerve fibers in mucosal regions of the distal aganglionic colon was evaluated semi-quantitatively in a double-blind investigation by four individuals. Mucosal regions were classified into 4 different fiber innervation grades according to absent, low, intermediate, and high innervation density (Supplementary Fig. 5a). Innervation grade 1 and 2 were grouped into fiber-low and 3 and 4 were grouped into fiber-high HSCR patients. For the quantitative measure of the AChE+ nerve fibers in the mucosal regions images were analyzed using brightfield microscope and CellSens Dimension 2.2 Software (Olympus). In average 6 cropped region of interest containing 10 epithelial crypts from distal colon, resulting in 60 crypts per patients, were analyzed. In total 12 patients (3 patients per innervation grade) were chosen according to the visual scoring. A defined manual threshold was applied on each cropped image and object counts were obtained by the Olympus CellSens dimension software (Supplementary Fig. 5a).

Isolation of mononuclear cells from colonic tissue

Colonic specimens were separated into rectum, sigmoid colon, colon descendens, transverse colon, and colon ascendens (distal to proximal) according to the length of the resected colon[117]. Excess fat was removed, and muscle layers were stripped from the mucosa. Mucosa and muscle tissue were minced and digested separately with collagenase D (1 mg/mL) and DNase I (4 µg/mL, both Roche Diagnostics, Basel?) in complete medium (RPMI-1640 supplemented with 10% FCS, 200 units

penicillin, 0.2 mg/mL streptomycin, 0.5 µg/mL amphotericin B, 80 µg/mL gentamycin, and 10 mM Hepes) at 37°C for 1 h under vigorous shaking. Digestion suspension was filtered through a 100 µm cell strainer, and cells were washed in complete medium. Suspension cells were resuspended in 20% percoll (3 mL) and underlaid with 40% percoll and 70% percoll (3 mL of each). Mononuclear cells were purified from the 40/70% percoll interface whereas epithelial cells were excluded in the 20/40% percoll interface. Cells were used freshly or were cryopreserved for further analysis.

Flow cytometry and fluorescence-activated cell sorting (FACS)

For intracellular cytokine detection, cells were restimulated in complete medium with phorbol 12-myristate 13-acetate (PMA; 150 ng/mL, Sigma-Aldrich) and ionomycin (750 ng/mL, Sigma-Aldrich) in the presence of GolgiStop™ and Brefeldin A (BD Biosciences) for 4 h at 37°C in a humidifying atmosphere. Viability was determined using LIVE/DEAD Fixable Near-IR dead cell stain (ThermoFisher). Cell surface markers were stained extracellularly (15 min, 4°C) in FACS buffer (PBS supplemented with 2% fetal calf serum, FCS), whereas cytokines and transcription factors were detected intracellularly using Cytofix/Cytoperm (BD Biosciences) or Foxp3/transcription factor staining buffer set (eBioscience), respectively. Unspecific Fcγ receptor binding was blocked by human Fc block (CD16/CD32). Lineage cocktail for innate lymphoid cells (ILC) contained markers for T cells (CD3, TCRα/β; TCRγ/δ), NK T cells (CD56), B cells (CD19), dendritic cells, monocytes, MΦ (CD11c, CD14, CD16), and mast cells (FcεRI). Cells were analyzed using FACS Canto II (BD Biosciences) and FlowJo software (TreeStar Inc.). MΦ were sorted as viable $CD45^{+}HLA^{+}CD64^{+}$ using FACS Aria cell sorter flow cytometry (BD Biosciences). Supplementary Table 8 details the human specific antibodies.

RNA isolation and quantitative real-time PCR (qRT-PCR)

Colonic tissues samples (max. 30 mg) were homogenized in RLT lysis buffer containing 1% 2-mercaptoethanol (Sigma-Aldrich) using a tissue disruptor (IKA). Total RNA from tissue or cells was isolated using the RNAeasy Plus mini kit (QiAgen) and was reverse-transcribed using GoScript Reverse Transcription System (Promega). Subsequently, qRT-PCR was done using the ViiA7 RT-PCR system (Thermo Fisher Scientific) and FastStart Universal SYBR Green Master (Roche Diagnostics) according to the manufacturers' instructions. Relative gene expression was calculated using the $2^{-\Delta CT}$ method, with β2-microglobulin as housekeeping gene, and results were multiplied by a factor of 1000. Primer pairs were designed according to exon junction span using the clone manager software (Sci-Ed Software). Supplementary Table 9 details the human-specific primer pairs.

Luminex analysis and enzyme-linked immunosorbent assays (ELISA)

We homogenized colonic tissues samples in Tissue Extraction Reagent I (100 µL/10 mg; ThermoFisher) containing protease inhibitor cocktail (Sigma-Aldrich) using a tissue disruptor (IKA). Concentrations (pg/mL) of IL-6, IL-22, IL-1β, TNF-α, and IL-17 were determined using MILLIPLEX®MAP Human Cytokine/ Chemokine/Growth Factor Panel A Assay and Luminex xMAP technology (MAGPIXTM) according to the manufacturers' instructions. Samples were measured using xPONENT for MAGPIX software. IL-23 was determined in tissue lysates using Human IL-23 ELISA Ready-Set-Go according to the manufacturer's instructions. IL-23 ELISA was measured using a Synergy H4 Hybrid Reader and GEN5 2.00 software (BioTeK).

Generation of blood-derived M1 and M2 MΦ

Peripheral blood mononuclear cells (PBMCs) from healthy adult volunteers were isolated using the SepMate/Lymphoprep system (Stemcell) according to the user manual. For monocyte attachment, PBMCs were resuspended in RPMI (supplemented with 10% FCS, 200 units penicillin, and 0.2 mg/mL streptomycin) and seeded into T-75 flasks for 2 h at 37°C in a humidifying atmosphere. The attached monocytes were washed twice with PBS and then cultured for 10 days in M1 or M2 Macrophage Generation Medium DXF (Promocell) according to the manufacturer's instructions. On day 10, cells were detached by adding Accutase® cell detachment solution (Sigma-Aldrich), washed twice with RPMI, and used for further applications.

T cell conversion assay

Autologous naïve CD4 T cells were isolated from PBMCs using EasyStep Human naïve $CD4^+$ T cell Isolation Kit (Stemcell) according to instruction manuals. M1 or M2 MΦ (10^4/well/200 µL) were cocultured with autologous naive $CD4^+$ T cells (10^5/well/200 µL) in the presence of 5 µg/mL anti-human CD3 for 6 days at 37°C in a humidifying atmosphere. Alternatively, $CD4^+$ T cells were activated using anti-human CD3/CD28 activation Dynabeads (Life Technologies) in a 1:1 ratio. For T helper cell differentiation, we added the following cytokines: IL-2 (5 ng/mL) and TGF-β1 (2 ng/mL) for Treg conversion and TGF-β1 (2 ng/mL) and IL-6 (10 ng/mL) for Th17 differentiation. All recombinant human cytokines were purchased from Preprotech. On day 6, T cells were separated from MΦ or Dynabeads into a new well and restimulated with PMA (150 ng/mL) and ionomycin (750 ng/mL) in the presence of GolgiStop™ and Brefeldin A for 4 h at 37°C in a humidifying atmosphere. T cell subsets were subsequently analyzed by flow cytometry using fluorescent antibodies against human TCRα/β, CD4, and IL-17/Rorγt or CD25/Foxp3 for Th17 and Treg cell identification. Cytokines and transcription factors were detected intracellularly using

transcription factor buffer set (BD Biosciences) according to the manufacturer's instructions. Frequencies of single subsets were determined as percentages of viable CD4/TCRα/β positive T cells. Ratios of Th17/Treg frequencies were calculated.

Immunofluorescence and colocalization studies

Longitudinal colonic strips were washed in ice-cold PBS and embedded as a Swiss roll in Tissue-Tek® O.C.T. compound. For fluorescence staining of immune cells and cholinergic fibers, we established a modified protocol of the anti-mouse HRP-AEC staining kit (R&D). All steps were performed at room temperature. Between all steps, the tissues were washed three times for 10 min in PBS and antibodies/streptavidin/4',6-diamidine-2'-phenylindole dihydrochloride (DAPI) were diluted in antibody diluent. Briefly, cryosections (5 µm) were fixed with 4% paraformaldehyde (PFA) for 5 min, followed by a blocking step with serum blocking reagent (15 min). Subsequently avidin and biotin were blocked using Avidin Blocking Reagent (15 min) followed by Biotin Blocking Reagent (15 min). Primary antibodies, purified mouse IgG2b anti-human AChE, together with purified mouse IgG1 anti-human CD64 or mouse IgG1 anti-human CD3-A488 or mouse IgG2a anti-human β3tubulin, were incubated for 1 h. CD64, AChE, β3tubulin, TH, nNOS, S100b, and VIP were detected by secondary antibodies goat anti-mouse IgG1 A488, goat anti-mouse IgG2b biotin, goat anti-mouse IgG2a A647 or IgG2b A647, goat anti-mouse IgG2a A555, goat anti-mouse IgG2a A555, goat anti-mouse IgG1 A555, and goat anti-guinea pig A555, respectively. IL-23p19 was directly PE-labeled. Biotin was visualized by streptavidin-Cy3 incubation for 30 min. Finally, nuclei were visualized by DAPI staining (3 min; 0.5 µg/mL), and slides were mounted using Prolong Diamond Antifade Mountant (Life Technologies). Secondary antibody controls were

included as negative controls. Images were taken by a fluorescence microscope (BX43 Olympus) and analyzed using CellSense (Olympus) and Fiji. Supplementary Table 8 details the antibodies used for histology. Fast-scanning confocal microscopy was performed with a Zeiss LSM880 Airyscan inverted system. Images were acquired and processed using Zen Black with a 63x plan apochromatic oil immersion objective DIC M27(NA1.4) using the three respective Ar-lasers 561 nm, 488 nm, and 405 nm in 4 frames average fast mode. The acquisition parameters and settings of the images were verified for the absence of crosstalk between Green and Red excitation and gain of the different lasers was always set at the same values for all acquisitions. Negative staining controls (secondary antibodies only) were used to determine pixel intensity background for the quantification. Images of fiber-high and fiber-low tissues were used for acquisition. Using a Fiji software macro, we quantified the colocalization pixel intensity between MΦ (or T cells) and AChE fibers. Briefly, images were created by multiplying and subsequent automated thresholding of the respective channels. Regions of interest containing MΦ (or T cells) were manually annotated in the raw data. The sum of colocalized pixel values contained within 100 to 200 annotated MΦ (or T cells) per patient tissue were measured on a sum projection image. Data are shown as raw integrated density (RawIntDen).

For the quantification of IL-23, images recorded under a 20x objective were analyzed using CellSense Software (Olympus) and Cellprofiler-3.1.9. To quantify IL-23$_+$ MΦ in tissue of different patient groups (4 fiber-low, 4 fiber-high), 4 to 8 regions per patient from rectum and sigmoid colon were used. Primary objects were defined by nuclear DAPI staining. Secondary object was defined by extracellular CD64 expression using the watershed module after applying a global threshold for improved cell identification. IL23 positive cells were identified as a second primary object (IL23$_+$),

using Three classes Otsu thresholding method, and subsequently related to CD64 MΦ. Frequencies of IL-23+ MΦ (IL23+CD64+) were shown as the percentage of total MΦ.

16s rRNA Fluorescence in situ hybridization

The FISH procedure was performed in 5 µm rectum/sigmoid colon Swiss roll cryosections. Colonic tissue sections were fixed with 4% PFA for 20 min on ice followed by a wash step in PBS. Slides were dipped into ice-cold methanol prior to hybridization with Cy3-labeled EUB338 sense probe (GCT GCC TCC CGT AGG AGT) or EUB338 anti-sense probe (ACT CCT ACG GGA GGC AGC) as negative control, in hybridization buffer (20 mM Tris-HCl; 0.9% NaCl; 0.1% SDS) at 48°C for 16 h. Slides were washed twice in hybridization wash buffer (20 mM Tris-HCl; 0.9% NaCl; pH 7.2) for 30 min at 48°C and subsequently mounted with ProLong Gold Antifade Mountant with DAPI (Life Technologies) and evaluated with a fluorescence microscope (BX43 Olympus). Images were analyzed using CellSense Software (Olympus) and Fiji software. To quantify the bacterial translocation in the different patient groups, 4 to 6 regions per picture from rectum and sigmoid colon were used, and corresponding sites were used for anti-sense probe. On average, 2000 DAPI+ cells/region were then processed using Cellprofiler software. In brief, primary objects were defined by nuclear DAPI staining. After masking the nuclei, a second primary object (Eub338_bacteria) based on nuclear Eub338 expression was defined and related to DAPI+ cells. Global Otsu two classes thresholding method was applied for DAPI nuclei staining, and manual thresholding for Eub338 was used before masking the nuclei to subtract the background. The anti-sense probe was running in parallel under the same pipeline, and results were subtracted from the sense probe.

Frequencies of translocated bacteria (16sRNA+/DAPI+) were expressed as the percentage of total DAPI+ cells.

16S rDNA gene sequencing

For 16s rDNA microbial analysis, we used colonic cryosections (100 µm). Extraction, lysis, and DNA isolation were done using Fast DNA Stool Mini Kit (Qiagen) according to the manufacturer's instructions. Bead beating was run on a fastprep24 instrument (MPBiomedicals; 2 cycles of 45 s at speed 4, followed by 2 cycles of 45 s at speed 5) in 2 mL screwcap tubes containing 0.1 mm zirconia beads (0.3 g) and 2.3 mm zirconia beads (0.36 g). The whole raw extract was prepared for DNA isolation. Concentration of the isolated DNA was determined with PicoGreen measurement (Quant-iT™ PicoGreen™ dsDNA Assay Kit, Thermo Fisher), and integrity was checked by agarose gel electrophoresis.

The Illumina MiSeq platform and a v2 500 cycles kit were used to sequence the PCR libraries. The produced paired-end reads which passed Illumina's chastity filter were subjected to de-multiplexing and trimming of Illumina adaptor residuals using Illumina's real time analysis software included in the MiSeq reporter software v2.6 (no further refinement or selection). The quality of the reads was checked with the software FastQC version 0.11.7. The locus-specific V34 primers were trimmed from the sequencing reads with the software Cutadapt v1.14. Paired-end reads were discarded if the primer could not be trimmed. Trimmed-forward and reverse reads of each paired-end read were merged to reform the sequenced molecule *in silico*, considering a minimum overlap of 15 bases using the software USEARCH version 10.0.240. Merged sequences were then quality-filtered, allowing a maximum of one expected error per merged read and also discarding those containing ambiguous bases. The remaining reads were denoised using the UNOISE algorithm

implemented in USEARCH to form operational taxonomic units (OTUs) discarding singletons and chimeras in the process. OTUs were compared to the reference sequences of the SILVA 16S database, and taxonomies were predicted considering a minimum confidence threshold of 0.6 using the SINTAX algorithm implemented in USEARCH. Alpha diversity was estimated using the Richness (Observed), Shannon and Simpson indices. Beta diversity was calculated using the Unifrac distance method on the basis of normalized OTU abundance counts per sample. These sample distances were then used in a detrended correspondence analysis (DCA) to reveal possible patterns of inter-sample relations. Alpha and beta diversity calculations and the rarefaction analysis were performed with the R software package phyloseq v1.22.3. To detect differentially abundant OTUs depending on collected sample metadata (e.g., medication, environmental conditions), differential OTU analysis on normalized abundance counts was performed with the R software package DESeq2 v1.18.1. Libraries, sequencing, and data analysis described in this section were performed by Microsynth AG (Balgach, Switzerland).

RNA-seq analysis

FACS sorted viable MΦ (300-3000 cells) as well as blood-derived M1 and M2 MΦ (100000 cells) were used for RNA-seq analysis. RNA was isolated using RNeasy micro kit (Qiagen). RNA samples were quantified using Qubit 2.0 Fluorometer (Life Technologies, Carlsbad, CA, USA), and RNA integrity was checked with Agilent TapeStation (Agilent Technologies, Palo Alto, CA, USA). RNA library preparations, sequencing reactions, and initial bioinformatics analysis were conducted at GENEWIZ, LLC. (South Plainfield, NJ, USA). The SMART-Seq v4 Ultra Low input kit for sequencing was used for full-length cDNA synthesis and amplification (Clontech, Mountain View, CA) according to the manufacturer’s protocol. Illumina Nextera XT

library was used for library preparation. Briefly, cDNA was fragmented, and adaptors were added using transposase, followed by limited-cycle PCR to enrich and add index to the cDNA fragments. Final libraries were analyzed on the Agilent TapeStation for library sizing and quantified using the Qubit dsDNA HS assay kit and by qPCR using the KAPA library quantification kit. The sequencing libraries were multiplexed and clustered on two lanes of a flow cell. After clustering, the flow cell was loaded on the Illumina HiSeq instrument according to the manufacturer's instructions. The samples were sequenced using a 2x150 Paired End (PE) configuration. Image analysis and base calling were conducted by the HiSeq Control Software (HCS). Raw sequence data (.bcl files) generated from Illumina HiSeq were converted into fastq files and de-multiplexed using Illumina's bcl2fastq 2.17 software. One mismatch was allowed for index sequence identification. After investigating the quality of the raw data, sequence reads were trimmed to remove possible adapter sequences and nucleotides with poor quality using Trimmomatic v.0.36. The trimmed reads were mapped to the human reference genome available on ENSEMBL using the STAR aligner v.2.5.2b. The STAR aligner uses a splice aligner that detects splice junctions and incorporates them to help align the entire read sequences. BAM files were generated as a result of this step. Unique gene hit counts were calculated by using featureCounts of the Subread package v.1.5.2. Only unique reads that fell within exon regions were counted. After extraction of gene hit counts, the gene hit counts table was used for downstream differential expression analysis. All statistical analyses were performed using R project software. Comparison of gene expression between the groups of samples was performed with the package DESeq2. The Wald test was used to generate p-values and Log2 fold changes. Genes with adjusted p-values < 0.05 and absolute log2 fold changes > 1 were regarded as differentially

expressed genes for each comparison. The statistically significant set of genes was subjected to a gene ontology analysis by implementing the software GeneSCF. The mgi GO list was used to cluster the set of genes based on their biological process and to determine their statistical significance. A PCA analysis was performed using the plotPCA function of the DESeq2 R package. The plot shows the samples in a 2D plane spanned by their first two principal components. The top 500 genes, selected by highest row variance, were used to generate the plot.

Statistical analysis

Data were analyzed using Prism GraphPad 6.0 software and Stata (StataCorp. 2015. Stata Statistical Software: Release 15. College Station, TX: StataCorp LP). Data are reported as the means ± standard error of the mean (SEM). Statistical significance was determined using unpaired nonparametric two-tailed Mann-Whitney test, and differences were considered statistically significant with * $p \leq 0.05$; ** $p \leq 0.01$; *** $p \leq 0.001$, and **** $p \leq 0.0001$. Unless otherwise noted, figures show pooled patient data from several independent experiments or a representative of repeated experiments. The characteristics and risk factors of study participants were compared between fiber-low versus fiber-high HSCR patient groups, and between subjects with enterocolitis versus no enterocolitis during follow-up, using two-sided Wilcoxon rank-sum test and $\chi 2$-test, as appropriate.

Data availability

The datasets generated and analyzed during the current study have been deposited in NCBI Sequence Read Archive under the accession code PRJNA552657 (RNA-seq datasets) and PRJNA550537 (16s rDNA datasets). All other study-related data are available from the corresponding author upon reasonable request.

841

References

1 Demehri, F. R., Halaweish, I. F., Coran, A. G. & Teitelbaum, D. H. Hirschsprung-associated enterocolitis: pathogenesis, treatment and prevention. *Pediatr Surg Int* **29**, 873-881, doi:10.1007/s00383-013-3353-1 (2013).

2 Austin, K. M. The pathogenesis of Hirschsprung's disease-associated enterocolitis. *Semin Pediatr Surg* **21**, 319-327, doi:10.1053/j.sempedsurg.2012.07.006 (2012).

3 Wang, J. S., Lee, H. C., Huang, F. Y., Chang, P. Y. & Sheu, J. C. Unexpected mortality in pediatric patients with postoperative Hirschsprung's disease. *Pediatr Surg Int* **20**, 525-528, doi:10.1007/s00383-004-1213-8 (2004).

4 Aslam, A., Spicer, R. D. & Corfield, A. P. Turnover of radioactive mucin precursors in the colon of patients with Hirschsprung's disease correlates with the development of enterocolitis. *J Pediatr Surg* **33**, 103-105 (1998).

5 Mattar, A. F., Coran, A. G. & Teitelbaum, D. H. MUC-2 mucin production in Hirschsprung's disease: possible association with enterocolitis development. *J Pediatr Surg* **38**, 417-421; discussion 417-421, doi:10.1053/jpsu.2003.50071 (2003).

6 Soeda, J., O'Briain, D. S. & Puri, P. Regional reduction in intestinal neuroendocrine cell populations in enterocolitis complicating Hirschsprung's disease. *J Pediatr Surg* **28**, 1063-1068 (1993).

7 Imamura, A., Puri, P., O'Briain, D. S. & Reen, D. J. Mucosal immune defence mechanisms in enterocolitis complicating Hirschsprung's disease. *Gut* **33**, 801-806 (1992).

8 Turnock, R. R., Spitz, L. & Strobel, S. A study of mucosal gut immunity in infants who develop Hirschsprung's-associated enterocolitis. *J Pediatr Surg* **27**, 828-829 (1992).

9 O'Donnell, A. M., Nakamura, H., Tomuschat, C., Marayati, N. F. & Puri, P. Altered expression of KCNG3 and KCNG4 in Hirschsprung's disease. *Pediatr Surg Int* **35**, 193-197, doi:10.1007/s00383-018-4394-2 (2019).

10 Hardy, S. P., Bayston, R. & Spitz, L. Prolonged carriage of Clostridium difficile in Hirschsprung's disease. *Arch Dis Child* **69**, 221-224, doi:10.1136/adc.69.2.221 (1993).

11 Shen, D. H. *et al.* Detection of intestinal bifidobacteria and lactobacilli in patients with Hirschsprung's disease associated enterocolitis. *World J Pediatr* **5**, 201-205, doi:10.1007/s12519-009-0038-x (2009).

12 Thomas, D. F., Fernie, D. S., Malone, M., Bayston, R. & Spitz, L. Association between Clostridium difficile and enterocolitis in Hirschsprung's disease. *Lancet* **1**, 78-79 (1982).

13 Ward, N. L., Pieretti, A., Dowd, S. E., Cox, S. B. & Goldstein, A. M. Intestinal aganglionosis is associated with early and sustained disruption of the colonic microbiome. *Neurogastroenterol Motil* **24**, 874-e400, doi:10.1111/j.1365-2982.2012.01937.x (2012).

14 Medrano, G. *et al.* B-lymphocyte-intrinsic and -extrinsic defects in secretory immunoglobulin A production in the neural crest-conditional deletion of

endothelin receptor B model of Hirschsprung-associated enterocolitis. *FASEB J*, fj201801913R, doi:10.1096/fj.201801913R (2019).

15 Cheng, Z. *et al.* Bacterial Microbiome Dynamics in Post Pull-Through Hirschsprung-Associated Enterocolitis (HAEC): An Experimental Study Employing the Endothelin Receptor B-Null Mouse Model. *Front Surg* **5**, 30, doi:10.3389/fsurg.2018.00030 (2018).

16 Bruder, E., Terracciano, L. M., Passarge, E. & Meier-Ruge, W. A. [Enzyme histochemistry of classical and ultrashort Hirschsprung's disease]. *Pathologe* **28**, 105-112, doi:10.1007/s00292-007-0901-2 (2007).

17 Stakenborg N., D. G. M., Boeckxstaens G.E., Matteoli G. The versatile role of the vagus nerve in the gastrointestinal tract. *EMJ Gastroenterol.*, 106-114 (2013).

18 Borovikova, L. V. *et al.* Vagus nerve stimulation attenuates the systemic inflammatory response to endotoxin. *Nature* **405**, 458-462, doi:10.1038/35013070 (2000).

19 Rosas-Ballina, M. *et al.* Acetylcholine-synthesizing T cells relay neural signals in a vagus nerve circuit. *Science* **334**, 98-101, doi:10.1126/science.1209985 (2011).

20 Ghia, J. E., Blennerhassett, P., Kumar-Ondiveeran, H., Verdu, E. F. & Collins, S. M. The vagus nerve: a tonic inhibitory influence associated with inflammatory bowel disease in a murine model. *Gastroenterology* **131**, 1122-1130, doi:10.1053/j.gastro.2006.08.016 (2006).

21 Bregeon, J. *et al.* Sacral nerve stimulation enhances early intestinal mucosal repair following mucosal injury in a pig model. *J Physiol* **594**, 4309-4323, doi:10.1113/JP271783 (2016).

22 Sun, P. *et al.* Involvement of MAPK/NF-kappaB signaling in the activation of the cholinergic anti-inflammatory pathway in experimental colitis by chronic vagus nerve stimulation. *PLoS One* **8**, e69424, doi:10.1371/journal.pone.0069424 (2013).

23 Gomez-Pinilla, P. J. *et al.* Prucalopride Activates the Intestinal Cholinergic Anti-Inflammatory Pathway and Prevents Postoperative Ileus. *Gastroenterology* **146**, S89-S89 (2014).

24 Di Giovangiulio, M. *et al.* Vagotomy affects the development of oral tolerance and increases susceptibility to develop colitis independently of the alpha-7 nicotinic receptor. *Mol Med* **22**, 464-476, doi:10.2119/molmed.2016.00062 (2016).

25 Matteoli, G. *et al.* A distinct vagal anti-inflammatory pathway modulates intestinal muscularis resident macrophages independent of the spleen. *Gut* **63**, 938-948, doi:10.1136/gutjnl-2013-304676 (2014).

26 Bastida, G. & Beltran, B. Ulcerative colitis in smokers, non-smokers and ex-smokers. *World J Gastroenterol* **17**, 2740-2747, doi:10.3748/wjg.v17.i22.2740 (2011).

27 Bonaz, B. *et al.* Chronic vagus nerve stimulation in Crohn's disease: a 6-month follow-up pilot study. *Neurogastroenterol Motil* **28**, 948-953, doi:10.1111/nmo.12792 (2016).

28 Cailotto, C. *et al.* Neuro-anatomical evidence indicating indirect modulation of macrophages by vagal efferents in the intestine but not in the spleen. *PLoS One* **9**, e87785, doi:10.1371/journal.pone.0087785 (2014).

29 Gautron, L. *et al.* Neuronal and nonneuronal cholinergic structures in the mouse gastrointestinal tract and spleen. *J Comp Neurol* **521**, 3741-3767, doi:10.1002/cne.23376 (2013).

30 Goverse, G., Stakenborg, M. & Matteoli, G. The intestinal cholinergic anti-inflammatory pathway. *J Physiol* **594**, 5771-5780, doi:10.1113/JP271537 (2016).

31 Kimura, H. *et al.* Neural anti-inflammatory action mediated by two types of acetylcholine receptors in the small intestine. *Sci Rep-Uk* **9**, doi:ARTN 5887 10.1038/s41598-019-41698-w (2019).

32 Szylberg, L. & Marszalek, A. Diagnosis of Hirschsprung's disease with particular emphasis on histopathology. A systematic review of current literature. *Prz Gastroenterol* **9**, 264-269, doi:10.5114/pg.2014.46160 (2014).

33 Wetherill, C. & Sutcliffe, J. Hirschsprung disease and anorectal malformation. *Early Hum Dev* **90**, 927-932, doi:10.1016/j.earlhumdev.2014.09.016 (2014).

34 Yoo, B. B. & Mazmanian, S. K. The Enteric Network: Interactions between the Immune and Nervous Systems of the Gut. *Immunity* **46**, 910-926, doi:10.1016/j.immuni.2017.05.011 (2017).

35 Revu, S. *et al.* IL-23 and IL-1beta Drive Human Th17 Cell Differentiation and Metabolic Reprogramming in Absence of CD28 Costimulation. *Cell Rep* **22**, 2642-2653, doi:10.1016/j.celrep.2018.02.044 (2018).

36 Burkett, P. R., Meyer zu Horste, G. & Kuchroo, V. K. Pouring fuel on the fire: Th17 cells, the environment, and autoimmunity. *J Clin Invest* **125**, 2211-2219, doi:10.1172/JCI78085 (2015).

37 Awasthi, A. *et al.* Cutting edge: IL-23 receptor gfp reporter mice reveal distinct populations of IL-17-producing cells. *J Immunol* **182**, 5904-5908, doi:10.4049/jimmunol.0900732 (2009).

38 Zhou, L. *et al.* IL-6 programs T(H)-17 cell differentiation by promoting sequential engagement of the IL-21 and IL-23 pathways. *Nat Immunol* **8**, 967-974, doi:10.1038/ni1488 (2007).

39 Korn, T., Bettelli, E., Oukka, M. & Kuchroo, V. K. IL-17 and Th17 Cells. *Annu Rev Immunol* **27**, 485-517, doi:10.1146/annurev.immunol.021908.132710 (2009).

40 Tosiek, M. J., Fiette, L., El Daker, S., Eberl, G. & Freitas, A. A. IL-15-dependent balance between Foxp3 and RORgammat expression impacts inflammatory bowel disease. *Nat Commun* **7**, 10888, doi:10.1038/ncomms10888 (2016).

41 Lee, S. H., Starkey, P. M. & Gordon, S. Quantitative analysis of total macrophage content in adult mouse tissues. Immunochemical studies with monoclonal antibody F4/80. *J Exp Med* **161**, 475-489 (1985).

42 Kuhl, A. A., Erben, U., Kredel, L. I. & Siegmund, B. Diversity of Intestinal Macrophages in Inflammatory Bowel Diseases. *Front Immunol* **6**, 613, doi:10.3389/fimmu.2015.00613 (2015).

43 Panea, C. *et al.* Intestinal Monocyte-Derived Macrophages Control Commensal-Specific Th17 Responses. *Cell Rep* **12**, 1314-1324, doi:10.1016/j.celrep.2015.07.040 (2015).

44 Hadis, U. *et al.* Intestinal tolerance requires gut homing and expansion of FoxP3+ regulatory T cells in the lamina propria. *Immunity* **34**, 237-246, doi:10.1016/j.immuni.2011.01.016 (2011).

45 Scott, C. L. *et al.* CCR2(+)CD103(-) intestinal dendritic cells develop from DC-committed precursors and induce interleukin-17 production by T cells. *Mucosal Immunol* **8**, 327-339, doi:10.1038/mi.2014.70 (2015).

46 Regoli, M., Bertelli, E., Gulisano, M. & Nicoletti, C. The Multifaceted Personality of Intestinal CX3CR1(+) Macrophages. *Trends Immunol* **38**, 879-887, doi:10.1016/j.it.2017.07.009 (2017).

47 Medina-Contreras, O. *et al.* CX3CR1 regulates intestinal macrophage homeostasis, bacterial translocation, and colitogenic Th17 responses in mice. *J Clin Invest* **121**, 4787-4795, doi:10.1172/JCI59150 (2011).

48 Dionne, S., Duchatelier, C. F. & Seidman, E. G. The influence of vitamin D on M1 and M2 macrophages in patients with Crohn's disease. *Innate Immun-London* **23**, 557-565, doi:10.1177/1753425917721965 (2017).

49 Muller, P. A. *et al.* Crosstalk between Muscularis Macrophages and Enteric Neurons Regulates Gastrointestinal Motility. *Cell* **158**, 1210, doi:10.1016/j.cell.2014.08.002 (2014).

50 Gabanyi, I. *et al.* Neuro-immune Interactions Drive Tissue Programming in Intestinal Macrophages. *Cell* **164**, 378-391, doi:10.1016/j.cell.2015.12.023 (2016).

51 De Schepper, S., Stakenborg, N., Matteoli, G., Verheijden, S. & Boeckxstaens, G. E. Muscularis macrophages: Key players in intestinal homeostasis and disease. *Cell Immunol* **330**, 142-150, doi:10.1016/j.cellimm.2017.12.009 (2018).

52 Wolf, Y. *et al.* Brown-adipose-tissue macrophages control tissue innervation and homeostatic energy expenditure. *Nat Immunol* **18**, 665-674, doi:10.1038/ni.3746 (2017).

53 Galitovskiy, V. *et al.* Cytokine-induced alterations of alpha7 nicotinic receptor in colonic CD4 T cells mediate dichotomous response to nicotine in murine models of Th1/Th17- versus Th2-mediated colitis. *J Immunol* **187**, 2677-2687, doi:10.4049/jimmunol.1002711 (2011).

54 Levite, M. Neurotransmitters activate T-cells and elicit crucial functions via neurotransmitter receptors. *Curr Opin Pharmacol* **8**, 460-471, doi:10.1016/j.coph.2008.05.001 (2008).

55 Lim, H. Y. *et al.* Hyaluronan Receptor LYVE-1-Expressing Macrophages Maintain Arterial Tone through Hyaluronan-Mediated Regulation of Smooth Muscle Cell Collagen. *Immunity* **49**, 1191, doi:10.1016/j.immuni.2018.12.009 (2018).

56 Stakenborg, N. *et al.* Preoperative administration of the 5-HT4 receptor agonist prucalopride reduces intestinal inflammation and shortens postoperative ileus via cholinergic enteric neurons. *Gut*, doi:10.1136/gutjnl-2018-317263 (2018).

57 Noh, H. *et al.* Beta 2-adrenergic receptor agonists are novel regulators of macrophage activation in diabetic renal and cardiovascular complications. *Kidney Int* **92**, 101-113, doi:10.1016/j.kint.2017.02.013 (2017).

58 Cardoso, V. *et al.* Neuronal regulation of type 2 innate lymphoid cells via neuromedin U. *Nature* **549**, 277-281, doi:10.1038/nature23469 (2017).

59 Klose, C. S. N. *et al.* The neuropeptide neuromedin U stimulates innate lymphoid cells and type 2 inflammation. *Nature* **549**, 282-286, doi:10.1038/nature23676 (2017).

60 Delgado, M. & Ganea, D. Vasoactive intestinal peptide: a neuropeptide with pleiotropic immune functions. *Amino Acids* **45**, 25-39, doi:10.1007/s00726-011-1184-8 (2013).

61 Chiu, I. M. *et al.* Bacteria activate sensory neurons that modulate pain and inflammation. *Nature* **501**, 52-57, doi:10.1038/nature12479 (2013).

62 Baliu-Pique, M., Jusek, G. & Holzmann, B. Neuroimmunological communication via CGRP promotes the development of a regulatory phenotype in TLR4-stimulated macrophages. *Eur J Immunol* **44**, 3708-3716, doi:10.1002/eji.201444553 (2014).

63 Assas, B. M., Pennock, J. I. & Miyan, J. A. Calcitonin gene-related peptide is a key neurotransmitter in the neuro-immune axis. *Front Neurosci* **8**, 23, doi:10.3389/fnins.2014.00023 (2014).

64 Riol-Blanco, L. *et al.* Nociceptive sensory neurons drive interleukin-23-mediated psoriasiform skin inflammation. *Nature* **510**, 157-161, doi:10.1038/nature13199 (2014).

65 Kashem, S. W. *et al.* Nociceptive Sensory Fibers Drive Interleukin-23 Production from CD301b+ Dermal Dendritic Cells and Drive Protective Cutaneous Immunity. *Immunity* **43**, 515-526, doi:10.1016/j.immuni.2015.08.016 (2015).

66 Earley, A. M., Graves, C. L. & Shiau, C. E. Critical Role for a Subset of Intestinal Macrophages in Shaping Gut Microbiota in Adult Zebrafish. *Cell Rep* **25**, 424-436, doi:10.1016/j.celrep.2018.09.025 (2018).

67 Rolig, A. S. *et al.* The enteric nervous system promotes intestinal health by constraining microbiota composition. *PLoS Biol* **15**, e2000689, doi:10.1371/journal.pbio.2000689 (2017).

68 Schneider, K. M. *et al.* Cx3cr1 Is a Gatekeeper for Intestinal Barrier Integrity: Limiting Steatohepatitis by Promoting Intestinal Homeostasis. *Journal of Hepatology* **62**, S225-S225, doi:Doi 10.1016/S0168-8278(15)30084-2 (2015).

69 Johnson, C. D. *et al.* Deletion of choline acetyltransferase in enteric neurons results in postnatal intestinal dysmotility and dysbiosis. *FASEB J* **32**, 4744-4752, doi:10.1096/fj.201701474RR (2018).

70 Niess, J. H. *et al.* CX3CR1-mediated dendritic cell access to the intestinal lumen and bacterial clearance. *Science* **307**, 254-258, doi:10.1126/science.1102901 (2005).

71 De Schepper, S. *et al.* Self-Maintaining Gut Macrophages Are Essential for Intestinal Homeostasis. *Cell* **175**, 400-415 e413, doi:10.1016/j.cell.2018.07.048 (2018).

72 Avetisyan, M. *et al.* Muscularis macrophage development in the absence of an enteric nervous system. *P Natl Acad Sci USA*, 4696-4701, doi:10.1073/pnas.1802490115 (2018).

73 Bogunovic, M. *et al.* Origin of the Lamina Propria Dendritic Cell Network. *Immunity* **31**, 513-525, doi:10.1016/j.immuni.2009.08.010 (2009).

74 Bosmans, G. *et al.* Vagus nerve stimulation dampens intestinal inflammation in a murine model of experimental food allergy. *Allergy*, doi:10.1111/all.13790 (2019).

75 van der Zanden, E. P. *et al.* Vagus nerve activity augments intestinal macrophage phagocytosis via nicotinic acetylcholine receptor alpha4beta2. *Gastroenterology* **137**, 1029-1039, 1039 e1021-1024, doi:10.1053/j.gastro.2009.04.057 (2009).

76 Klose, C. S. & Artis, D. Neuronal regulation of innate lymphoid cells. *Curr Opin Immunol* **56**, 94-99, doi:10.1016/j.coi.2018.11.002 (2019).

77 Stritesky, G. L., Yeh, N. & Kaplan, M. H. IL-23 promotes maintenance but not commitment to the Th17 lineage. *J Immunol* **181**, 5948-5955, doi:10.4049/jimmunol.181.9.5948 (2008).

78 Barrett, J. C. *et al.* Genome-wide association defines more than 30 distinct susceptibility loci for Crohn's disease. *Nature Genetics* **40**, 955-962, doi:10.1038/ng.175 (2008).

79 Galvez, J. Role of Th17 Cells in the Pathogenesis of Human IBD. *ISRN Inflamm* **2014**, 928461, doi:10.1155/2014/928461 (2014).

80 Franke, A. *et al.* Replication of signals from recent studies of Crohn's disease identifies previously unknown disease loci for ulcerative colitis. *Nature Genetics* **40**, 713-715, doi:10.1038/ng.148 (2008).

81 Duerr, R. H. *et al.* A genome-wide association study identifies IL23R as an inflammatory bowel disease gene. *Science* **314**, 1461-1463, doi:10.1126/science.1135245 (2006).

82 Gazouli, M. *et al.* NOD2/CARD15, ATG16L1 and IL23R gene polymorphisms and childhood-onset of Crohn's disease. *World J Gastroentero* **16**, 1753-1758, doi:10.3748/wjg.v16.i14.1753 (2010).

83 Lyakh, L., Trinchieri, G., Provezza, L., Carra, G. & Gerosa, F. Regulation of interleukin-12/interleukin-23 production and the T-helper 17 response in humans. *Immunol Rev* **226**, 112-131, doi:DOI 10.1111/j.1600-065X.2008.00700.x (2008).

84 Gerosa, F. *et al.* Differential regulation of interleukin 12 and interleukin 23 production in human dendritic cells. *Journal of Experimental Medicine* **205**, 1447-1461, doi:10.1084/jem.20071450 (2008).

85 Mortha, A. *et al.* Microbiota-Dependent Crosstalk Between Macrophages and ILC3 Promotes Intestinal Homeostasis. *Science* **343**, 1477-+, doi:ARTN 1249288

10.1126/science.1249288 (2014).

86 Schulz, O. *et al.* Intestinal CD103(+), but not CX3CR1(+), antigen sampling cells migrate in lymph and serve classical dendritic cell functions. *Journal of Experimental Medicine* **206**, 3101-3114, doi:10.1084/jem.20091925 (2009).

87 Chiu, I. M. *et al.* Bacteria activate sensory neurons that modulate pain and inflammation. *Nature* **501**, 52-+, doi:10.1038/nature12479 (2013).

88 Heuckeroth, R. O. Hirschsprung disease - integrating basic science and clinical medicine to improve outcomes. *Nat Rev Gastroenterol Hepatol* **15**, 152-167, doi:10.1038/nrgastro.2017.149 (2018).

89 Tilghman, J. M. *et al.* Molecular Genetic Anatomy and Risk Profile of Hirschsprung's Disease. *N Engl J Med* **380**, 1421-1432, doi:10.1056/NEJMoa1706594 (2019).

90 Ibiza, S. *et al.* Glial-cell-derived neuroregulators control type 3 innate lymphoid cells and gut defence. *Nature* **535**, 440-+, doi:10.1038/nature18644 (2016).

91 Rozakis-Adcock, M. *et al.* Association of the Shc and Grb2/Sem5 SH2-containing proteins is implicated in activation of the Ras pathway by tyrosine kinases. *Nature* **360**, 689-692, doi:10.1038/360689a0 (1992).

92 Zhang, Y. *et al.* GDF15 Regulates Malat-1 Circular RNA and Inactivates NFkappaB Signaling Leading to Immune Tolerogenic DCs for Preventing Alloimmune Rejection in Heart Transplantation. *Front Immunol* **9**, 2407, doi:10.3389/fimmu.2018.02407 (2018).

93 Wang, W. *et al.* GDF11 Antagonizes Psoriasis-like Skin Inflammation via Suppression of NF-kappaB Signaling Pathway. *Inflammation* **42**, 319-330, doi:10.1007/s10753-018-0895-3 (2019).

94 Wilson, A. M. *et al.* Neuropilin-1 expression in adipose tissue macrophages protects against obesity and metabolic syndrome. *Sci Immunol* **3**, doi:10.1126/sciimmunol.aan4626 (2018).

95 Aherne, C. M. *et al.* Neuronal guidance molecule netrin-1 attenuates inflammatory cell trafficking during acute experimental colitis. *Gut* **61**, 695-705, doi:10.1136/gutjnl-2011-300012 (2012).

96 Ranganathan, P., Jayakumar, C., Li, D. Y. & Ramesh, G. UNC5B receptor deletion exacerbates DSS-induced colitis in mice by increasing epithelial cell apoptosis. *J Cell Mol Med* **18**, 1290-1299, doi:10.1111/jcmm.12280 (2014).

97 Hu, S. & Zhu, L. Semaphorins and Their Receptors: From Axonal Guidance to Atherosclerosis. *Front Physiol* **9**, 1236, doi:10.3389/fphys.2018.01236 (2018).

98 Ji, J. D., Park-Min, K. H. & Ivashkiv, L. B. Expression and function of semaphorin 3A and its receptors in human monocyte-derived macrophages. *Hum Immunol* **70**, 211-217, doi:10.1016/j.humimm.2009.01.026 (2009).

99 Suzuki, K. *et al.* Semaphorin 7A initiates T-cell-mediated inflammatory responses through alpha1beta1 integrin. *Nature* **446**, 680-684, doi:10.1038/nature05652 (2007).

100 Xie, J. & Wang, H. Semaphorin 7A as a potential immune regulator and promising therapeutic target in rheumatoid arthritis. *Arthritis Res Ther* **19**, 10, doi:10.1186/s13075-016-1217-5 (2017).

101 Frykman, P. K. *et al.* Characterization of Bacterial and Fungal Microbiome in Children with Hirschsprung Disease with and without a History of Enterocolitis: A Multicenter Study. *Plos One* **10**, doi:ARTN e0124172 10.1371/journal.pone.0124172 (2015).

102 Thomas, D. F. M., Malone, M., Fernie, D. S., Bayston, R. & Spitz, L. Association between Clostridium-Difficil and Enterocolitis in Hirschsprungs-Disease. *Lancet* **1**, 78-79 (1982).

103 Saleh, M. M. *et al.* Colitis-Induced Th17 Cells Increase the Risk for Severe Subsequent Clostridium difficile Infection. *Cell Host & Microbe* **25**, 756-+, doi:10.1016/j.chom.2019.03.003 (2019).

104 Schirmer, M. *et al.* Linking the Human Gut Microbiome to Inflammatory Cytokine Production Capacity. *Cell* **167**, 1125-1136 e1128, doi:10.1016/j.cell.2016.10.020 (2016).

105 Vincent, C. *et al.* Bloom and bust: intestinal microbiota dynamics in response to hospital exposures and Clostridium difficile colonization or infection. *Microbiome* **4**, 12, doi:10.1186/s40168-016-0156-3 (2016).

106 Vincent, C. *et al.* Reductions in intestinal Clostridiales precede the development of nosocomial Clostridium difficile infection. *Microbiome* **1**, 18, doi:10.1186/2049-2618-1-18 (2013).

107 Stokholm, J. *et al.* Cesarean section changes neonatal gut colonization. *J Allergy Clin Immunol* **138**, 881-889 e882, doi:10.1016/j.jaci.2016.01.028 (2016).

108 Shin, H. *et al.* The first microbial environment of infants born by C-section: the operating room microbes. *Microbiome* **3**, 59, doi:10.1186/s40168-015-0126-1 (2015).

109 Shi, Y. C. *et al.* Initial meconium microbiome in Chinese neonates delivered naturally or by cesarean section. *Sci Rep* **8**, 3255, doi:10.1038/s41598-018-21657-7 (2018).

110 Mueller, N. T. *et al.* Delivery Mode and the Transition of Pioneering Gut-Microbiota Structure, Composition and Predicted Metabolic Function. *Genes (Basel)* **8**, doi:10.3390/genes8120364 (2017).

111 Erickson, C. S. *et al.* Sacral neural crest-derived cells enter the aganglionic colon of Ednrb-/- mice along extrinsic nerve fibers. *J Comp Neurol* **520**, 620-632, doi:10.1002/cne.22755 (2012).

112 Pierre, J. F. *et al.* Intestinal dysbiosis and bacterial enteroinvasion in a murine model of Hirschsprung's disease. *J Pediatr Surg* **49**, 1242-1251, doi:10.1016/j.jpedsurg.2014.01.060 (2014).

113 Druckenbrod, N. R., Powers, P. A., Bartley, C. R., Walker, J. W. & Epstein, M. L. Targeting of endothelin receptor-B to the neural crest. *Genesis* **46**, 396-400, doi:10.1002/dvg.20415 (2008).

114 Georgeson, K. E. & Robertson, D. J. Laparoscopic-assisted approaches for the definitive surgery for Hirschsprung's disease. *Semin Pediatr Surg* **13**, 256-262 (2004).

115 Chen, Y. *et al.* Transanal endorectal pull-through versus transabdominal approach for Hirschsprung's disease: a systematic review and meta-analysis. *J Pediatr Surg* **48**, 642-651, doi:10.1016/j.jpedsurg.2012.12.036 (2013).

116 Romero, P. *et al.* Outcome of transanal endorectal vs. transabdominal pull-through in patients with Hirschsprung's disease. *Langenbecks Arch Surg* **396**, 1027-1033, doi:10.1007/s00423-011-0804-9 (2011).

117 Struijs, M. C., Diamond, I. R., de Silva, N. & Wales, P. W. Establishing norms for intestinal length in children. *J Pediatr Surg* **44**, 933-938, doi:10.1016/j.jpedsurg.2009.01.031 (2009).

Acknowledgment

We thank all the patients and their parents as well as volunteer blood donors for their contribution. We also thank T. Lopes, E. Traunecker, and L. Raeli at the Flow Cytometry Facility of the Department of Biomedicine (Basel) for cell sorting, A. Loynton-Ferrand, K. Schleicher, and O. Biehlmaier at the Imaging Core Facility of the Biocenter (Basel) for assistance in confocal microscopy, D. Calabrese at the Histology Facility of the Department of Biomedicine (Basel) for histological support, N. Ritz and A. Zelmer at University Children's Hospital (Basel) for Luminex analysis, P. Weigold at Microsynth AG (Balgach) for microbiome analysis, and S. Rogers at MediWrite (Basel) for her excellent manuscript revision.

This work was supported by the "Stay on track" grant (awarded to S.K.) and the "Nachwuchsförderung klinische Forschung" grant (awarded to S.K.; DMS2343) from the University of Basel, Switzerland.

Author contributions

S.K.: study design; design, execution, and supervision of the experiments; data acquisition, analysis, and interpretation; writing and revision of the manuscript; V.G-F.: execution of the experiments; data acquisition and analysis; contribution to manuscript drafting; U.K.: execution of the experiments; data acquisition and analysis; M.M.: execution of the experiments; data acquisition and analysis of retrospective patient cohort; J.U.: statistical analysis; E.B.: acquisition of patient samples; revision of the manuscript; U.S., S.J.T., T.K., E.S, P.S., D.C., P.R., B.R., and NIG Study Group: recruitment, characterization, and follow-up of patients; revision of the manuscript S.H-C.: study design, recruitment, characterization, and follow-up of patients; revision of the manuscript.

Competing interests

The authors declare no competing interests.

Figure legends

Fig. 1 Distribution of neuronal innervation and fiber scoring of HSCR patients

a, Schematic representation of neuronal innervation in non-HSCR (control group) and HSCR patients. Images (5 µm colonic cryosections) show immunohistochemical tubulin staining of ganglionic CD region (non-HSCR) or AChE staining of aganglionic rectum region (HSCR). CD regions of HSCR patients were ganglionic or aganglionic dependent on the length of aganglionosis (see Supplementary Table 1). Rec (rectum); SC (sigmoid colon); CD (colon descendens). **b-c**, Longitudinal colonic strips were rolled up from the distal to proximal ends and cryopreserved as a 'Swiss roll'. Cholinergic nerve fibers were visualized in 5 µm cryosections by AChE immunohistochemical staining using brightfield microscopy. The presence and density of AChE+ fibers in rectum (1 REC) and sigmoid colon (2 SC) were evaluated by four individuals. **b**, Representative image of a fiber-low colonic sections. **c**, Representative image of a fiber-high colonic section. Close-up view shows epithelial region from the different colonic segments.

Fig. 2 Mucosal cholinergic innervation in distal aganglionic colon of fiber high HSCR patient

a, Differently innervated colonic segments from aganglionic and ganglionic regions of HSCR patients and control patients used for subsequent laboratory analysis. Immunofluorescence (5 µm cryosections) of epithelial/mucosal region using tubulin (Alexa647, green), a general neuronal marker, and AChE (Cy3, red), a cholinergic marker. DAPI (blue) shows cell nuclei. Images were taken by fluorescence microscopy (20x, scale bar 50 µm) and processed by Fiji software. Encircled areas mark the lumen. Arrows mark cholinergic fibers; asterisk mark non-cholinergic fibers.

b, Immunofluorescence (5 µm Swiss roll cryosections) of aganglionic rectum region from a fiber-high patient using tubulin (Alexa647, green), a general neuronal marker, combined with VIP (vasoactive intestinal peptide; A555, red), labeling peptidergic neurons; TH (tyrosine hydroxylase; A555, red), labeling dopaminergic and adrenergic neurons; NOS (nitric oxide synthase, A555, red), labeling nitrinergic neurons and S100B (S100 calcium-binding protein B, A555, red), labeling glia cells. DAPI (blue) shows cell nuclei. Images were taken by fluorescence microscopy (20x, scale bar 50 µm) and processed by Fiji software. Close-up views (white boxes) show mucosal/epithelial region. **c-d**, Immunofluorescence (5 µm Swiss roll cryosections) of aganglionic rectum region from a fiber-high patient using secondary antibody controls.

Fig. 3 Cytokine profile and immune cell populations in colonic tissue

a, Quantitative RT-PCR analysis of total colonic tissue isolated from different aganglionic (AG) and ganglionic (G) colonic segments of HSCR and control patients. Fiber-low (n=31); fiber-high (n=13); AG CD (n=12); G CD (n=11); control CD (n=4). IL-17 expression was not detectable in 1 AG CD sample and in 1 G CD sample. IL-22 expression was not detectable in 2 G CD sample. **b,** Luminex analysis of total colonic tissue isolated from different aganglionic (AG) and ganglionic (G) colonic segments of HSCR and control patients. IL-23 was determined by ELISA. Fiber-low (n=30); fiber-high (n=13); AG CD (n=12); G CD (n=12); control CD (n=5). IL-17 protein expression was not detectable in 1 Fiber high sample. IL-22 protein expression was not detectable in 5 Fiber low; 3 Fiber high: 3 AG CD; 5G CD and 3 control CD samples. **c-e**, Flow cytometric analysis of mononuclear cells isolated from different aganglionic and ganglionic colonic segments of HSCR and control patients. **c**, Frequencies of IL-17$_+$ Th17 T cells were determined in viable CD3$_+$CD4$_+$

lymphocytes restimulated with PMA/Ionomycin (Supplementary Fig. 3a). **d**, Treg cells were defined as CD127^{-}Foxp3^{+} cells in unstimulated viable CD3^{+}CD4^{+} lymphocytes using Foxp3/transcription factor staining buffer set (Supplementary Fig. 3b). Fiber-low (n=30); fiber-high (n=13); AG CD (n=10); G CD (n=10); control CD (n=5) **e,** Th17/Treg ratio is shown. **f**, Frequencies of CD11c^{+} and CD14^{+} MΦ were evaluated in viable HLA^{+}CD64^{+} cells by flow cytometry (Supplementary Fig. 2d). Fiber-low (n=26); Fiber-high (n=13); AG CD (n=10); muscle (n=10); G CD (n=10); control CD (n=5). **g,** CD64^{+} MΦ were assessed by immunofluorescence in 5 µm colonic cryosections from a muscle region (left), a mucosal region from a fiber-low patient, and a mucosal region from fiber-high patient (right). Scale bar 30 µm (muscle) and 10 µm (fiber-low; fiber-high). Images from 3 fiber-high and 3 fiber-low patients were analyzed for MΦ shape. A total of 100-200 CD64^{+} cells per patient were counted and the percentage of bipolar cells calculated (bar graph). Scatter plots show means ± SEM. Significance was determined using unpaired nonparametric Mann-Whitney test (* $p \leq 0.05$; ** $p \leq 0.01$; *** $p \leq 0.001$). Source data are provided as a Source Data file.

Fig. 4 MΦ colocalize with cholinergic nerve fibers

a, Immunofluorescence of epithelial region in cryosections (5 µm, Swiss roll of rectum and sigmoid colon) of representative fiber-high and fiber-low patients. Anti-AChE (red); anti-CD64 or anti-CD3 (green); DAPI (blue). Image from muscle region (right) shows thick fiber bundles (AChE) together with CD64^{+} cells. Images were obtained by fluorescence (20x, scale bar 30 µm) and confocal (63x, scale bar 10 µm) microscopy and processed by Fiji software. **b**, Confocal immunofluorescence image of an intercrypt region from a fiber-high patient. Overlapping pixels (yellow, arrows) were visualized on a Z-projection image. See Supplementary movie.

c-d, Quantification of the pixel intensity colocalization of CD64+ MΦ **(c)** or CD3+ T cells **(d)** with AChE+ fibers was performed by a Fiji software macro. Confocal images from distal colon regions of fiber-low (n=4 for CD64; n=3 for CD3) and fiber-high (n=5 for CD64; n=3 for CD3) patients as well as from muscle regions of HSCR patients (n=2) were taken. The following negative staining controls were used: CD64-A488 **(c)** or CD3-A488 **(d)** with biotin + streptavidin-Cy3 and IgG1-A488 + biotin/streptavidin-Cy3 (n=2). Per patient (dot), 200-300 cells were analyzed. Scatter plots show mean raw integrated density (RawIntDen) ± SEM. **e**, CD64+ MΦ from 3 fiber-high patients were investigated with respect to bipolar (n=170) or round/stellate (n=152) morphological phenotype. Raw integrated density of colocalized pixels between CD64 and AChE are shown. Significance was determined using unpaired nonparametric Mann-Whitney test (* $p \leq 0.05$; **** $p \leq 0.0001$). Source data are provided as a Source Data file.

Fig. 5 Fiber-associated MΦ express diminished IL-23 levels

RNA sequencing was performed on sorted viable colonic MΦ (CD45+HLA+CD64+, Supplementary Fig.3d and Methods) and blood-derived M1 and M2 MΦ.

a, PCA plot shows similarity between the different populations based on their first two principal components. The top 500 genes, selected by highest row variance, were used. PC, principal component. Fiber-low (green, n=4); fiber-high (blue, n=5); muscle (red, n=3); M1 (black, n=3); M2 (grey, n=3). **b**, Normalized sequence reads of selected macrophage-related genes. Scatter plots show means ± SEM. Significance was determined using unpaired nonparametric Mann-Whitney test or unpaired t-test (for M1/M2 MΦ) (* $p \leq 0.05$; ** $p \leq 0.01$; *** $p \leq 0.001$) **c**, Global transcriptional changes between macrophages isolated from fiber-low colonic tissue and fiber-high colonic tissue visualized by a volcano plot. Genes with an adjusted

p-value < 0.05 and log2 fold change greater than 1 (red dots) and less than -1 (blue dots) are indicated. **d**, Heat map of differentially expressed genes (from b) between MΦ in fiber-low colonic tissue and fiber-high colonic tissue. Each column represents one patient. **e**, Normalized sequence reads of selected genes. Scatter plots show means ± SEM. Significance was determined using unpaired nonparametric Mann-Whitney test or unpaired t-test (for M1/M2 MΦ) (* $p \leq 0.05$; ** $p \leq 0.01$; *** $p \leq 0.001$). **f-g**, IL-23$^+$CD64$^+$ MΦ were assessed by immunofluorescence in 5 µm colonic cryosections. A representative image of mucosal/epithelial region from fiber-low tissue (**f**) and fiber-high tissue (**g)** is shown. Scale bar 30 µm. CD64 (A647, green); IL23p19-PE (red) **h**, Quantitative analysis of IL-23 expression in macrophages evaluated in images from 4 fiber-high and 4 fiber-low patients. A total of 900-4700 CD64$^+$ cells per patient were analyzed for IL-23 expression and the percentage of IL23$^+$CD64$^+$ cells (% of total macrophages) calculated. Scatter plots show means ± SEM. Significance was determined using unpaired nonparametric Mann-Whitney test (* $p \leq 0.05$). Source data are provided as a Source Data file.

Fig. 6 Receptors involved in macrophage-neuron crosstalk

a-e, Heat maps of selected genes possibly involved in macrophage-neuron crosstalk. Normalized reads are shown. RNA sequencing was performed on sorted viable colonic MΦ (CD45$^+$HLA$^+$CD64$^+$) from mucosa of fiber-low (n=4) and fiber-high (n=5) colonic tissue as well as muscle tissue (n=3). Heat maps show mean values of each group. **a**, Expression of nicotinic (CHRNA) and muscarinic (CHRM) ACh receptors. **b**, Expression of serotonergic (HTR) and catecholaminergic (ADRB) receptors. **c**, Expression of receptors for neuromedin U (NMUR1), vasoactive-intestinal-peptide (VIPR1), somatostatin (SSTR2), calcitonin-gene-related peptide (CALCRL/RAMP1). **d**, Expression of neurotrophins (bone-morphogenic proteins [BMP] and

growth/differentiation factors [GDF]) and neurotrophin receptors (NTRK2 binds brain-derived-neurotrophic factor (BDNF) and neurotrophin (NT)-4; GFRA2 and RET bind GDNF and neurturin. **e**, Expression of axon-guidance proteins and respective receptors. Semaphorins (SEMA) bind to plexins or neuropilin-1 (NRP1). UNC-5 represent the receptor for netrin. Receptor proteins ROBO1 and 3 bind slit proteins. Neogenin (Neo) receptor binds to repulsive guidance protein (RGM). Ephrins bind to Eph receptors EPHA and EPHB. **f**, Normalized sequence reads of selected genes. Scatter plots show means ± SEM. Significance was determined using unpaired nonparametric Mann-Whitney test (*$p \leq 0.05$). Source data are provided as a Source Data file.

Fig. 7 Colonic microbial dysbiosis in fiber-low colonic tissue from HSCR patients

a-d, 16S rRNA analysis of colonic tissue from aganglionic (fiber-low n=14; fiber-high n=11) and ganglionic (CD gang. n=4) segments of age-matched HSCR patients. **a**, Alpha diversity analysis show effects on observed operational taxonomic units (OTUs) and estimated OTU richness by Shannon and Simpson indices. **b**, Pie charts show microbial composition in each group on phylum level. **c**, Scatter plots show normalized reads of bacterial classes dedicated to respective phyla. Scatter blots show mean values ± SEM. Significance was determined using unpaired nonparametric Mann-Whitney test (* $p \leq 0.05$). **d**, Differential bacterial family analysis of fiber-low versus fiber-high groups. Asterisk mark significantly changed families with an adjusted p value< 0.05 (***$p= 4.01 \times 10^{-15}$; **$p= 2.08 \times 10^{-4}$; *$p= 0.022$). Families are assigned to respective phyla by color code. Source data are provided as a Source Data file.

Tab. 1 Risk factors for post-operative enterocolitis

a, Prospective HSCR patient cohort (n=42). Values are median (range) or number (percentage); (n): number of data available; length of aganglionosis: rectum (1), sigmoid colon (2), colon descendens (3), colon transversum (4), colon ascendens (5). Differences between enterocolitis development (yes/no) were tested with the Wilcoxon rank-sum test and χ2-test, as appropriate. No follow-up for patients no. 0023 and 0032 available**. b**, Retrospective HSCR patient cohort (n=29). Values are mean (SD), median (range), or number (percentage); n: number; SD: standard deviation. Differences between enterocolitis development (yes/no) were tested with the Wilcoxon rank-sum test and χ2-test, as appropriate. Source data are provided as a Source Data file.

Fig. 1 Distribution of neuronal innervation and fiber scoring of HSCR patients

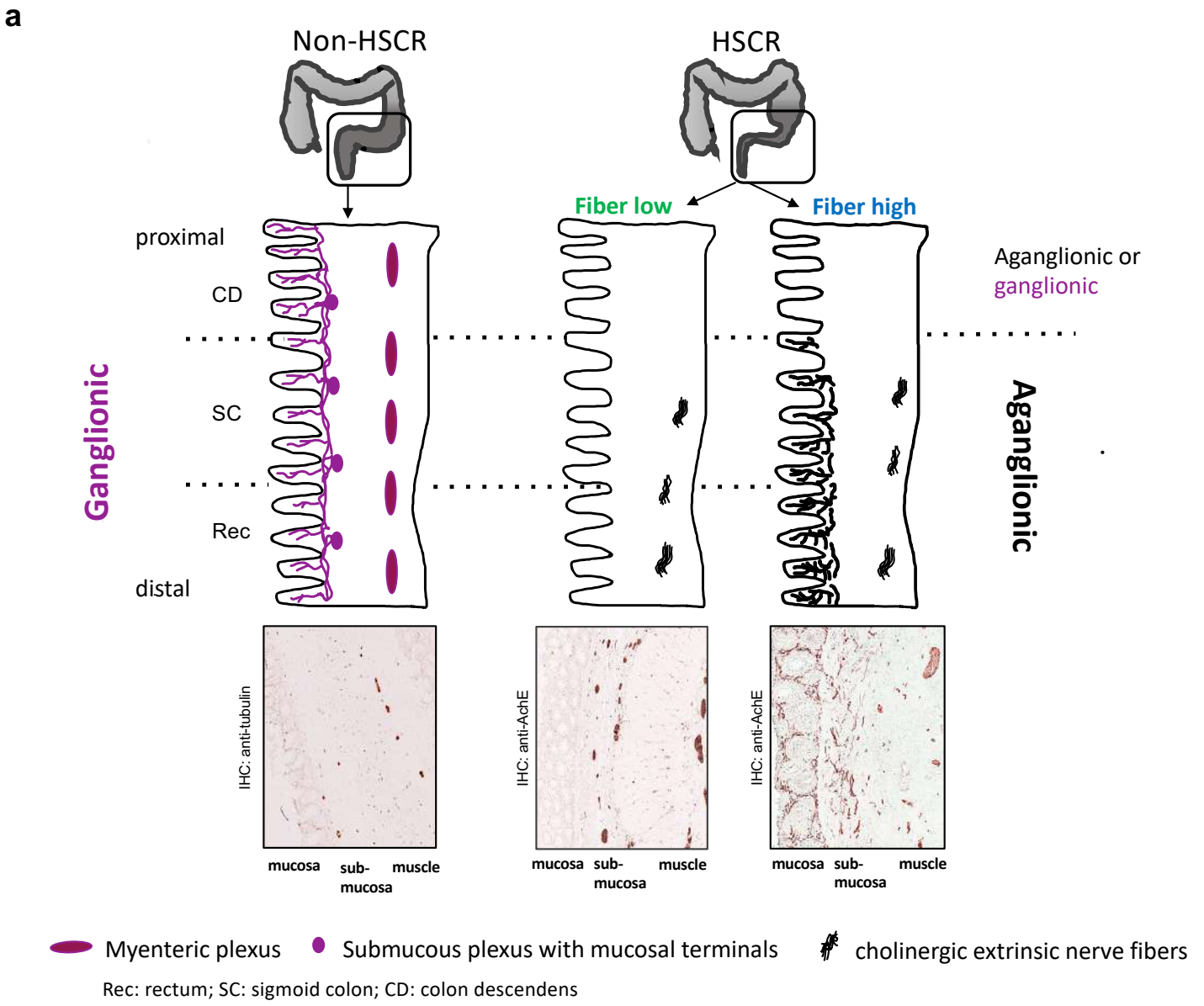

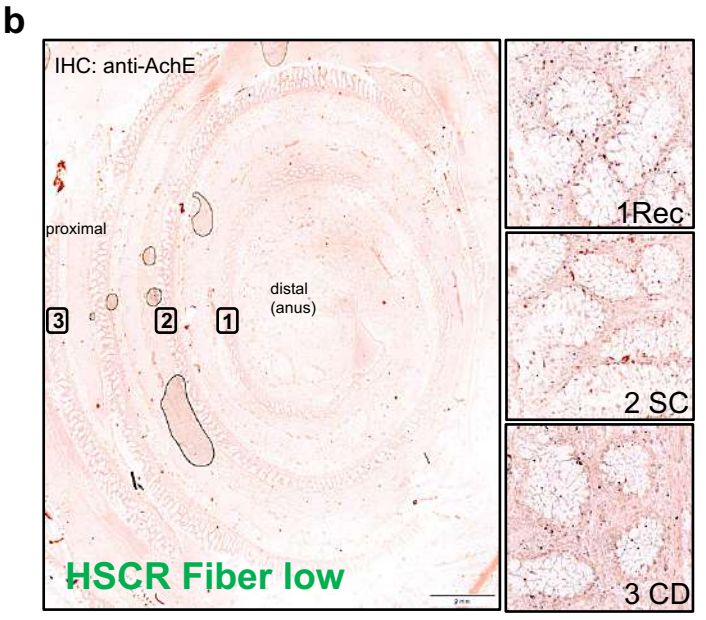

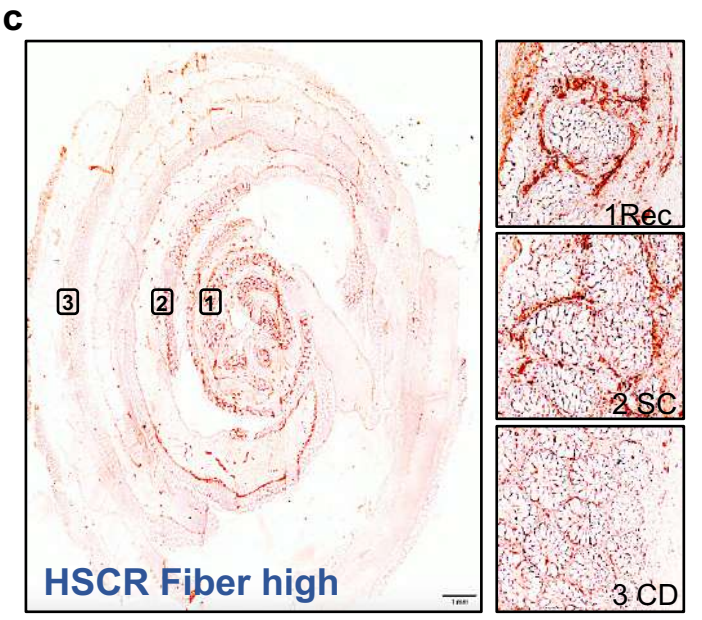

Fig. 2 Mucosal cholinergic innervation in distal aganglionic colon of fiber high HSCR patient

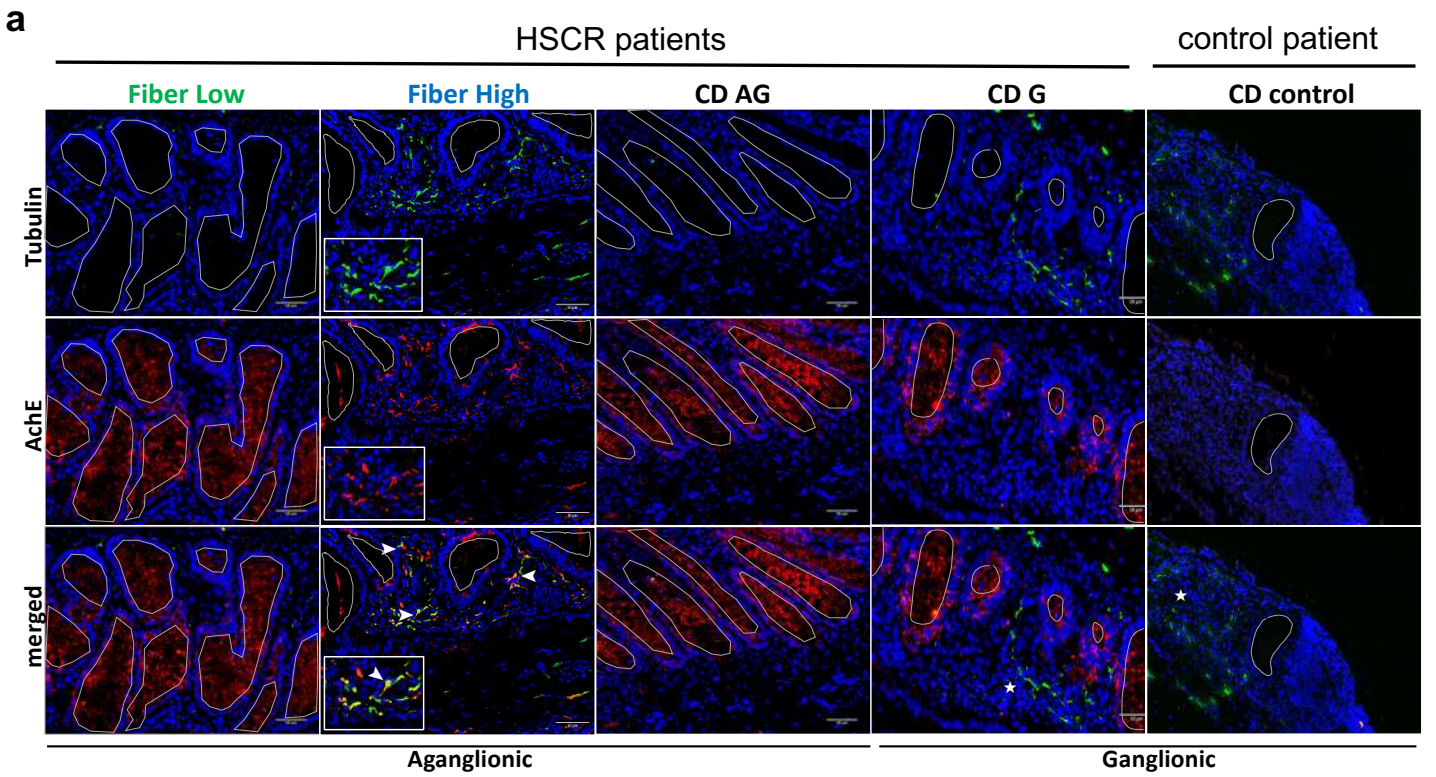

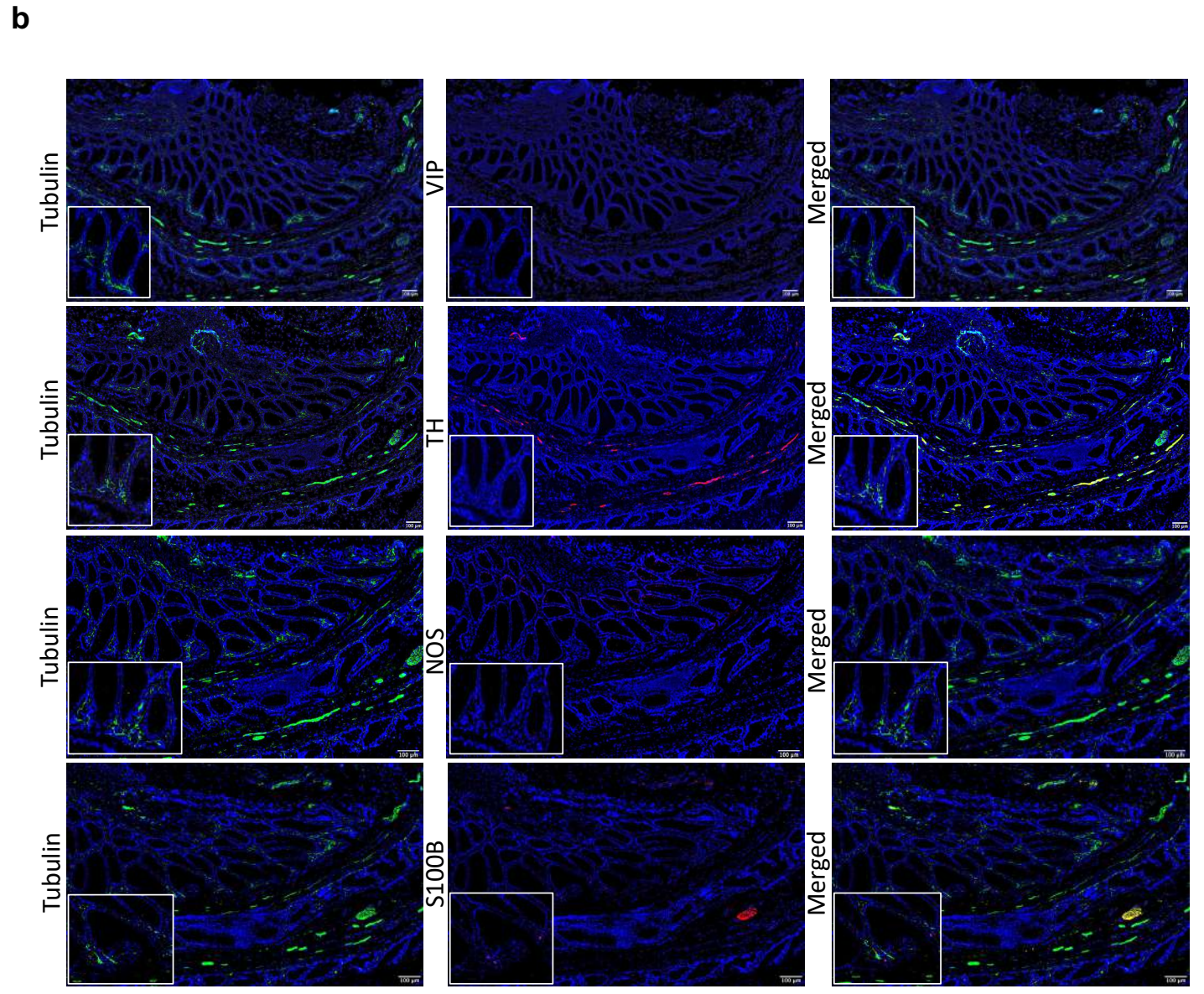

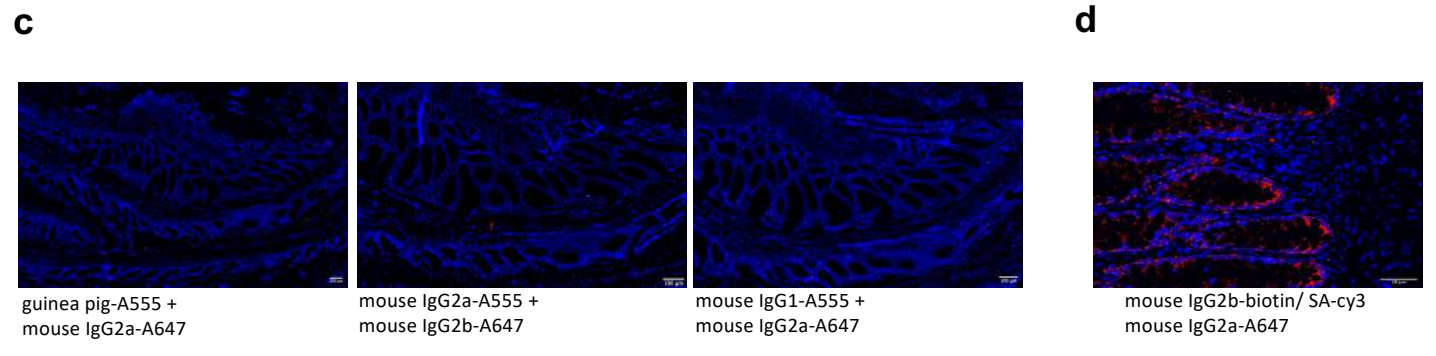

Fig. 3 Cytokine profile and immune cell populations in colonic tissue

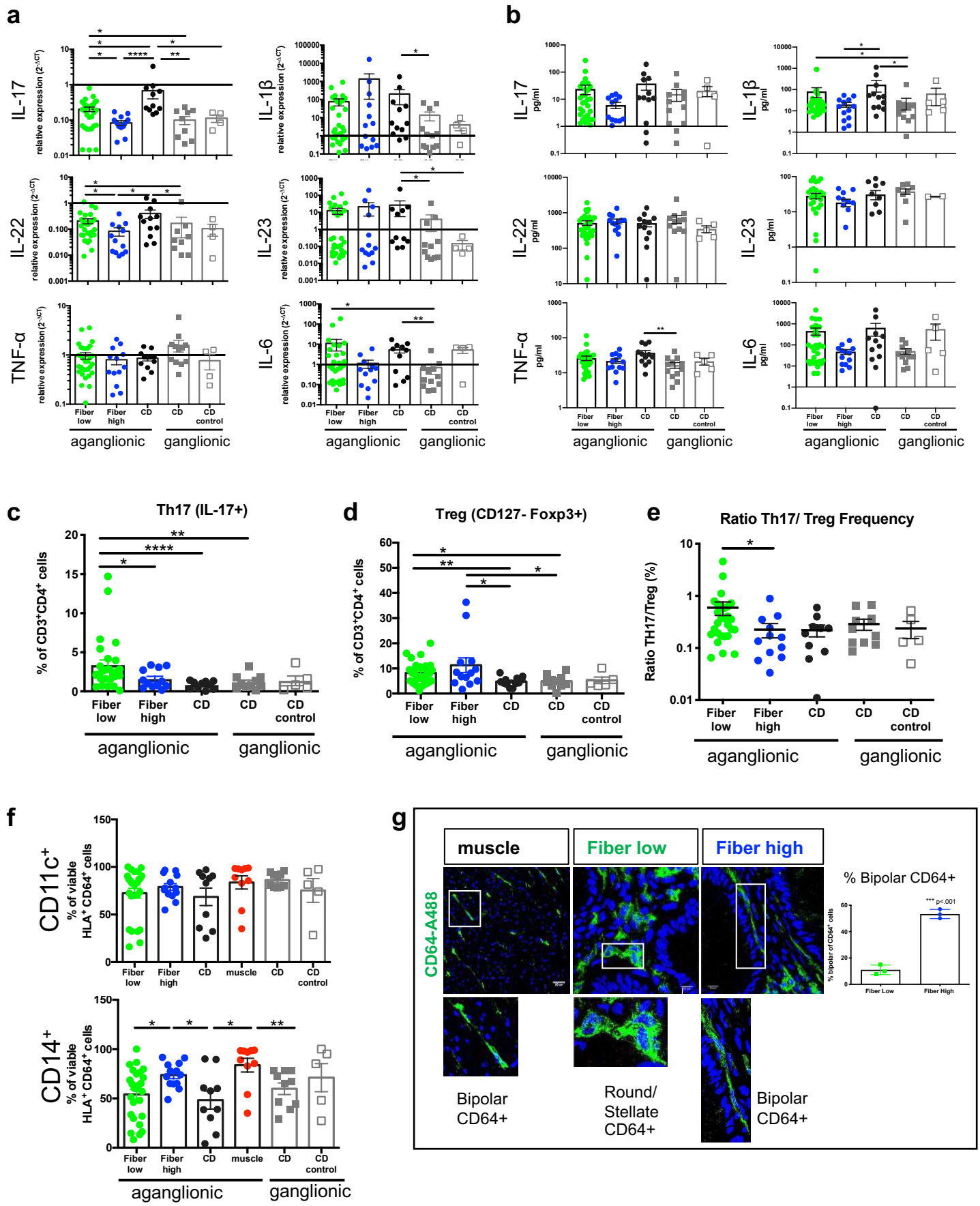

Fig. 4 Macrophages colocalize with cholinergic nerve fibers

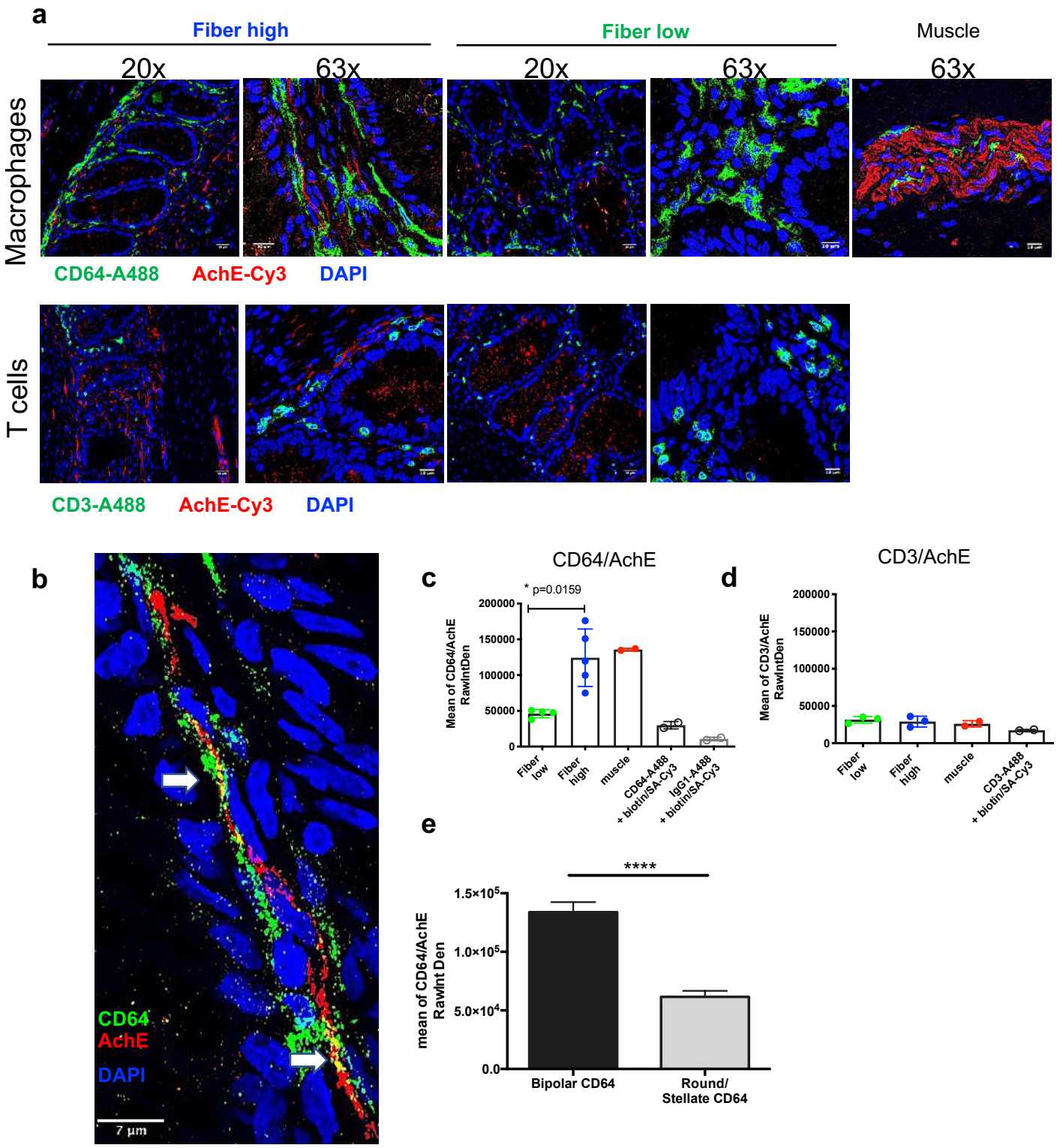

Fig. 5 Fiber-associated macrophages express diminished IL-23 levels

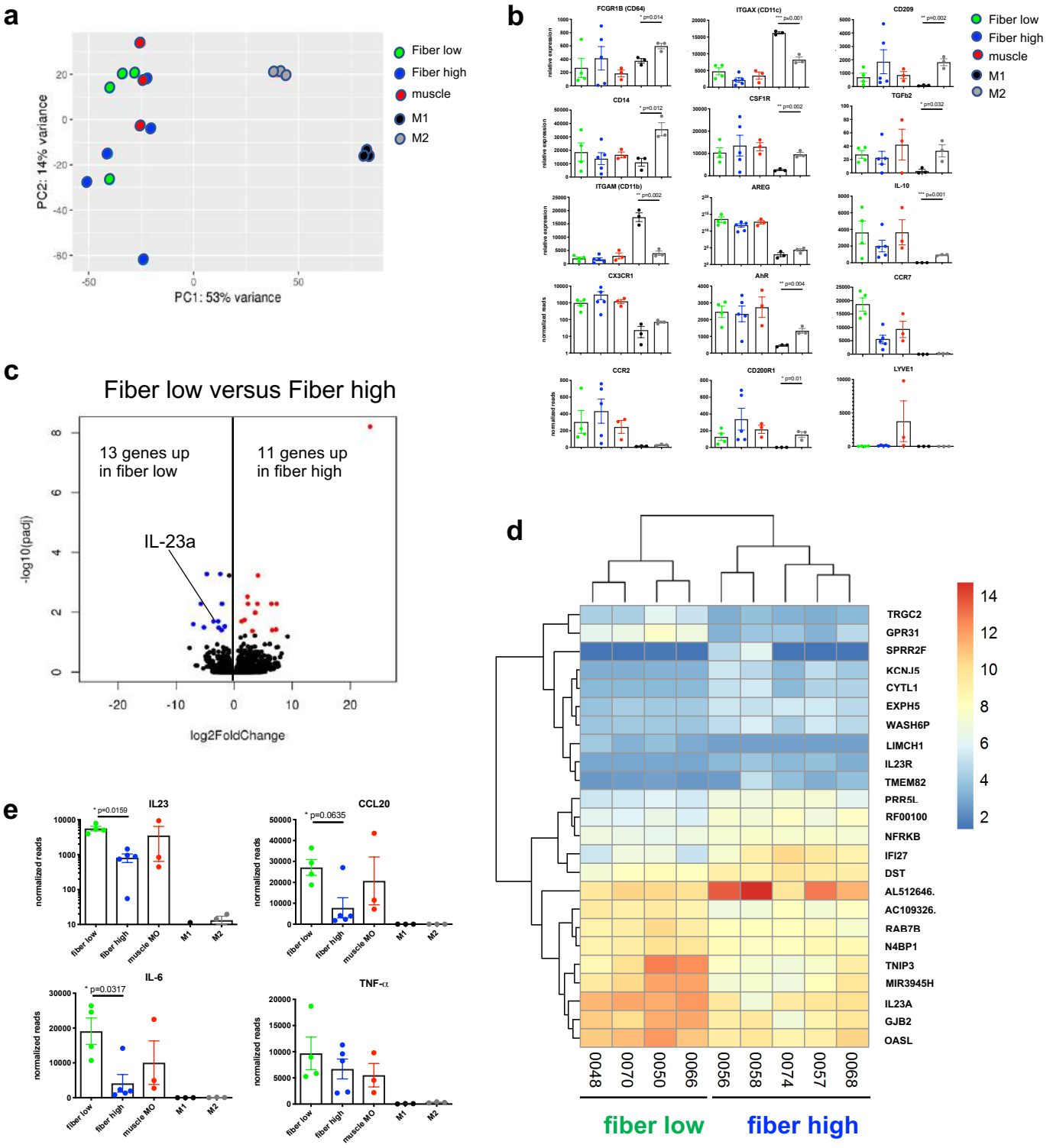

Fig. 6 Receptors involved in macrophage-neuron crosstalk

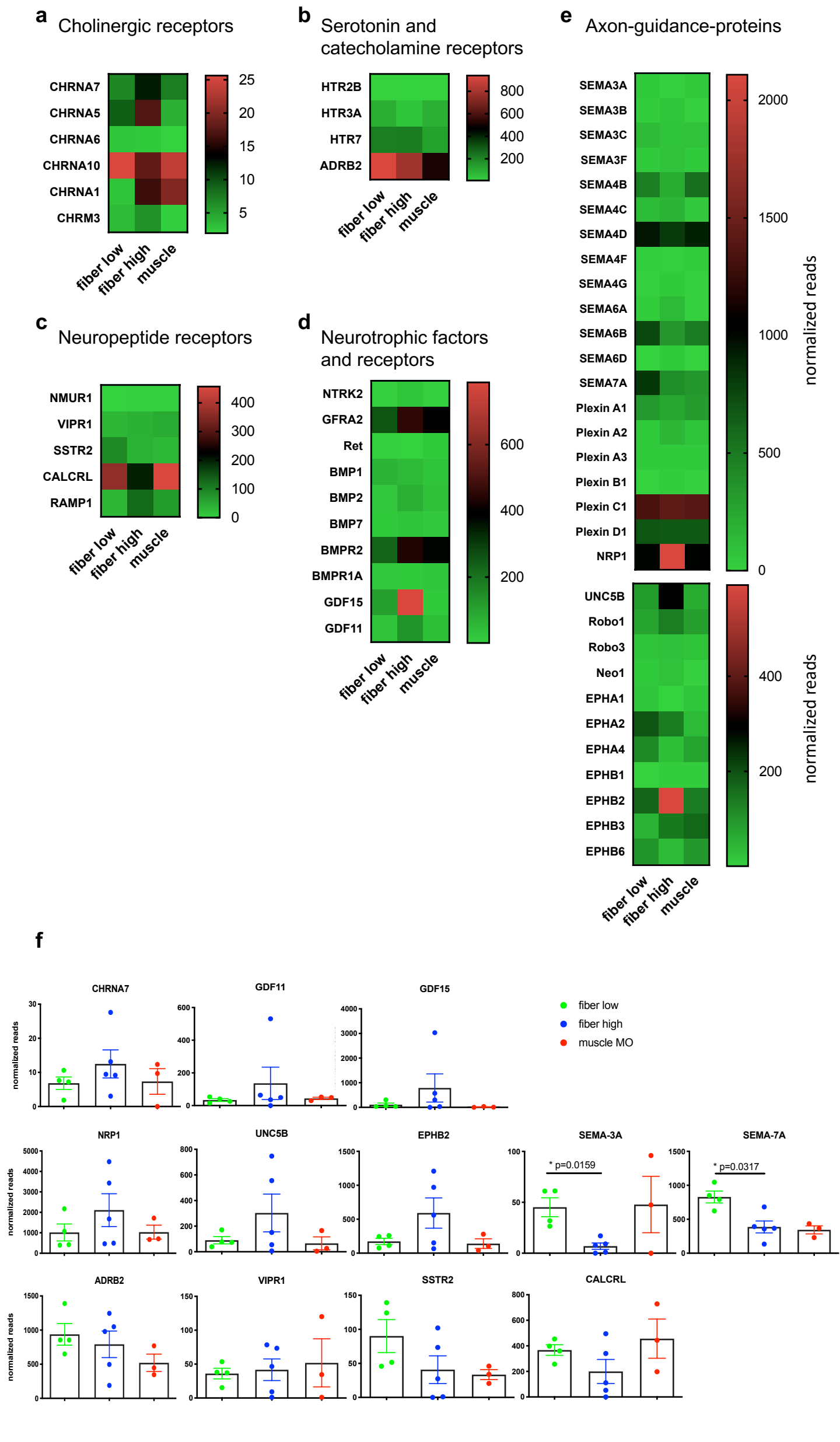

Fig. 7 Colonic microbial dysbiosis in fiber low colonic tissue from HD patients

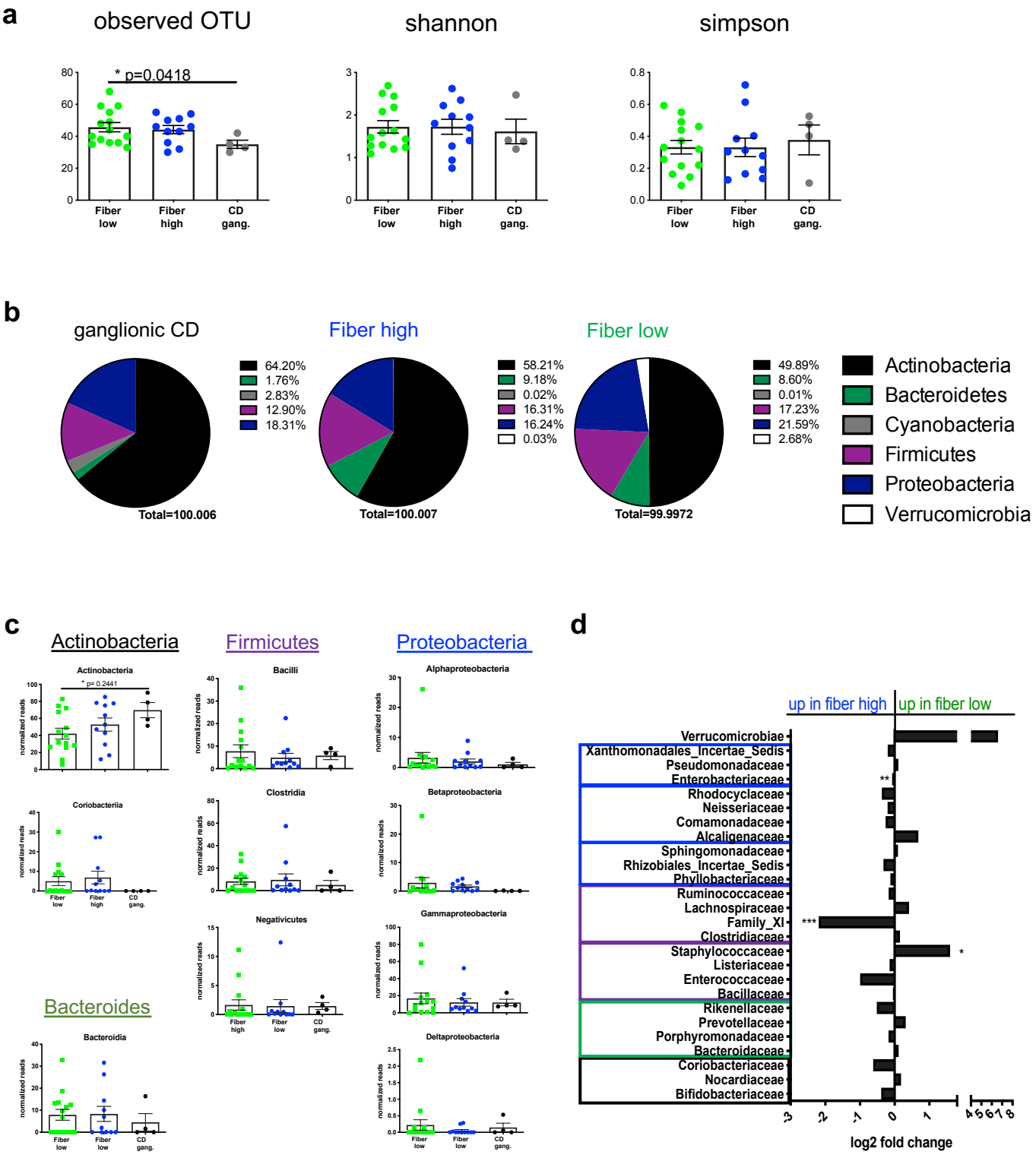

Table 1: Risk factors for post-operative enterocolitis development

a

Prospective HSCR patient cohort	**Enterocolitis**		**p-value**
Anthropometric data and potential risk factors, (n)	Yes n=9	No n=33	
Age at operation, months (42)	3 (1–127)	5 (2–70)	0.211
Sex, male (42)	7 (78)	27 (81)	0.784
Preterm birth (38)	2 (22)	1 (3)	0.068
Operation procedure trans-anal (42)	8 (89)	29 (88)	0.934
Length of aganglionosis (42)	1 (1-5)	2 (1-5)	0.061
Pets (37)	1 (11)	11 (39)	0.116
Patient living in rural area (40)	3 (33)	17 (55)	0.256
Antibiotic treatment (38)	2 (22)	3 (10)	0.357
Siblings (39)	8 (89)	22 (73)	0.331
Breastfed at operation (39)	9 (100)	27 (90)	0.323
Maternal age at delivery, years (35)	27 (23-39)	29 (21-43)	0.788
Parental smoking (38)	4 (44)	5 (17)	0.094
Caesarean Section (38)	6 (75)	8 (27)	0.012
Maternal Allergy (38)	1 (11)	8 (31)	0.236
Fiber low (30)	7 (78)	23 (70)	0.634
Fiber high(12)	2 (22)	10 (30)	0.634

b

	Enterocolitis		**p-value**
Retrospective HSCR patient cohort	Yes (n=14)	No (n=15)	
Age at operation, months	4 (1–48)	9 (1–171)	0.229
Sex, male	11 (79)	14 (93)	0.249
Preterm birth	1 (7)	1 (7)	0.960
Antibiotic treatment	10 (7)	11 (73)	0.909
Caesarean Section	7 (50)	5 (33)	0.124
Fiber low	12 (86)	3 (20)	<0.001
Fiber high	2 (14)	12 (80)	<0.001